Regulation of Ebola GP conformation and membrane binding by the chemical environment of the late endosome

Aastha Jain[1], Ramesh Govindan[1,2], Alexander Berkman[1], Jeremy Luban[3,4], Natasha D. Durham[1], James B. Munro[1,4*]

[1]Department of Microbiology and Physiological Systems, UMass Chan Medical School, Worcester, MA, USA

[2]Medical Scientist Training Program, Tufts University School of Medicine, Boston, MA

[3]Program in Molecular Medicine, UMass Chan Medical School, Worcester, MA

[4]Department of Biochemistry and Molecular Biotechnology, UMass Chan Medical School, Worcester, MA

*Correspondence: james.munro@umassmed.edu

Abstract

Interaction between the Ebola virus envelope glycoprotein (GP) and the endosomal membrane is an essential step during virus entry into the cell. Acidic pH, Ca^{2+}, and removal of the glycan cap from GP have been implicated in mediating the GP-membrane interaction. However, the molecular mechanism by which these factors regulate the conformational changes that enable engagement of GP with the target membrane is unknown. Here, we apply fluorescence correlation spectroscopy (FCS) and single-molecule Förster resonance energy transfer (smFRET) to elucidate how the chemical environment of the late endosome promotes GP-membrane interaction, thereby facilitating virus entry. We first investigate the role of anionic phospholipids, phosphatidylserine (PS) and bis(monoacylglycero)phosphate (BMP), which are found in the membrane of the late endosome. We find that these lipids enable robust binding of GP to membranes in a pH- and Ca^{2+}-dependent manner. We then identify residues in GP that sense pH and trigger conformational changes that make the fusion loop available for insertion into the membrane. Molecular dynamics (MD) simulations suggest the structural basis for pH-trigger conformational changes. We similarly confirm residues in the fusion loop that mediate GP's interaction with Ca^{2+}, which likely promotes local conformational changes in the fusion loop and mediates electrostatic interactions with the anionic phospholipids. Collectively, our results provide a mechanistic understanding of how the environment of the late endosome regulates the timing and efficiency of virus entry.

32 **Introduction**

33 Ebola (EBOV) is an enveloped, negative-stranded RNA virus, which causes disease in humans with an
34 average case fatality rate of 50% (Salata et al., 2019). Since its discovery, there have been several
35 outbreaks of EBOV disease in sub-Saharan Africa with the most recent being in September 2022
36 ("Ebola returns: back to square one", 2022). Incidences of repetitive outbreaks, changes in virulence,
37 or emergence of resistance could reduce the effectiveness of currently approved vaccination and
38 treatment regimes. Therefore, a better understanding of the EBOV entry mechanism, an under-
39 utilized drug target, would aid in the development of effective prophylactic and treatment
40 interventions.

41 The EBOV fusion and entry process is not fully decoded. It is well known that the EBOV envelope
42 glycoprotein (GP), present on surface of the virion, mediates virus entry in host cells. GP is a timer of
43 heterodimers with each protomer consisting of two subunits, GP1 and GP2, which are linked by
44 disulfide bonds (J. E. Lee et al., 2008). The virions attach to the host cell surface via GP1 interaction
45 with C-type lectins and phosphatidylserine receptors, and are internalized by macropinocytosis
46 (Mulherkar et al., 2011; Nanbo et al., 2010). Once inside the endosomes, cathepsins B and L
47 proteolytically remove the mucin-like domain and glycan cap from GP1, enabling its binding to the
48 endosomal receptor, the Niemann-Pick C1 (NPC1) cholesterol transporter (Carette et al., 2011;
49 Chandran et al., 2005; Côté et al., 2011; Miller et al., 2012). Additional factors yet to be identified are
50 likely required to trigger the conformational changes in GP that are necessary to promote fusion of
51 the viral and endosomal membranes (Fénéant et al., 2019).

52 While in the endocytic pathway, acidification of the endosomal lumen and Ca^{2+} play critical, but poorly
53 defined roles in promoting EBOV entry (Brecher et al., 2012; Das et al., 2020; Nathan et al., 2020;
54 Saeed et al., 2010; Sakurai et al., 2015). In a study conducted on the isolated GP fusion loop (residues
55 507-560), conserved residues were mutated to identify pH sensors that trigger membrane binding (J.
56 Lee et al., 2016). Mutation of H516 reduced lipid mixing promoted by the fusion loop by 80% in an *in*
57 *vitro* assay. However, no difference in virus-like particle entry into mammalian cells could be seen with
58 respect to wild type. This study suggested that instead of a single amino acid residue acting as a pH
59 sensor, the effect of changes in pH is spread over multiple residues that collectively influence the
60 conformational changes of GP. Another study investigated the interaction of Ca^{2+} ions with anionic
61 residues flanking the fusion loop (Nathan et al., 2020). Residues D522 and E540 were especially crucial
62 for interaction of the isolated fusion loop with Ca^{2+}, which enhances membrane binding. Our previous
63 single-molecule Förster resonance energy transfer (smFRET) experiments on trimeric GP on the
64 surface of pseudoviral particles demonstrated that low pH and Ca^{2+} play a critical role in promoting

65 conformational changes in GP that correlate with lipid mixing (Das et al., 2020). While prior studies
66 had suggested residues in the fusion loop that are involved in sensing pH and Ca^{2+}, the role of these
67 residues in mediating conformational changes of trimeric GP was not evaluated. Nor has it been
68 determined how additional residues outside of the fusion loop might allosterically regulate
69 conformational dynamics of GP and fusion loop-mediated membrane binding.

70 Lipids in host cell membranes can facilitate virus attachment and regulate fusion. Lipid content of
71 endosomes is important in sorting of enveloped viruses into specific compartments and avoiding
72 premature fusion (Mazzon & Mercer, 2014). The late endosomal membrane is rich in anionic lipids,
73 phosphatidylserine (PS) and bis(monoacylglycero)phosphate (BMP) (Hullin-Matsuda et al., 2014;
74 Urade et al., 1988). BMP is essential for fusion of viruses such as Dengue, Lassa, Uukuniemei and
75 vesicular stomatitis virus that enter cells through the endocytic route (Bitto et al., 2016; Markosyan et
76 al., 2021; Matos et al., 2013; Nour et al., 2013; Zaitseva et al., 2010). However, a role for BMP in EBOV
77 GP entry could not be verified using a cell-cell fusion assay (Fénéant et al., 2019). This may indicate
78 that the plasma membrane lacks other lipid or protein components, which are specific to the
79 endosome and essential for EBOV GP-mediated fusion. Therefore, whether endosomal lipids play a
80 role in EBOV entry remains an open question.

81 In the present study, we sought to elucidate the mechanistic basis for how the chemical features of
82 the late endosome enable GP to engage the target membrane prior to fusion. To probe the ability of
83 trimeric GP to bind membranes of distinct composition, we developed a fluorescence correlation
84 spectroscopy (FCS) assay. FCS provides quantitative information on the diffusion of molecules in
85 solution. In comparison to conventional pull-down or membrane flotation methods, FCS has high
86 spatio-temporal resolution, requires low sample quantity, and provides rapid experimental
87 throughput (Betaneli et al., 2019). Our results indicate that anionic lipids PS and BMP, enhanced the
88 extent of membrane binding of GP at acidic pH and in presence of Ca^{2+}. smFRET imaging indicated that
89 acidic pH and Ca^{2+} destabilized the pre-fusion conformation, allowing the fusion loop to move away
90 from its hydrophobic cleft to a position where it can engage the membrane. The presence of the target
91 membrane captured the fusion loop in a position distal to the base of the GP trimer. The results of
92 mutagenesis support a model in which pH- and Ca^{2+}-sensing residues tune the responsiveness of GP
93 to the chemical environment of the late endosome, ensuring proper timing of conformational changes
94 necessary for fusion.

95 **Results**

96 ***Anionic lipids and Ca^{2+} mediate GP-membrane binding at acidic pH***

97 We first sought to test the hypothesis that coordination of Ca^{2+} in the fusion loop of GP might aid in
98 engagement of GP with anionic phospholipids found in the late endosome. To this end, we developed
99 an FCS assay to monitor GP-membrane interactions. We prepared liposomes to mimic the endosomal
100 membrane using phosphatidylcholine (PC), PS, BMP, and cholesterol (Ch). The trimeric ectodomain of
101 GP (GPΔTM) from the Mayinga strain of EBOV, lacking the transmembrane domain and the mucin-like
102 domain was expressed and purified in Expi293 cells. A foldon trimerization domain was introduced at
103 the C-terminus to preserve the trimeric form of GPΔTM. GP1 and GP2 in GPΔTM were site-specifically
104 labelled with Cy5 using an enzymatic labelling approach (Materials and Methods) (Durham et al.,
105 2020). We noted that thermolysin, which is commonly used to remove the glycan cap from GP1 in
106 place of the endosomal cathepsin proteases, led to removal of the fluorophore. To alleviate this off-
107 target effect of thermolysin, the thermolysin cleavage site was replaced with the HRV3C protease
108 recognition sequence. This enabled equivalent removal of the glycan cap from GP1 (forming GP^{CL}) and
109 left the Cy5 labelling intact (**Figure S1A**). In a pseudovirion infectivity assay, introduction of the HRV3C
110 sequence left GP 85% functional as compared to wild-type GP (**Figure S1B**).

111 As measured by FCS, the labelled GP^{CL} diffused as a single homogeneous species with a diffusion time
112 of 0.308 ± 0.007 ms (**Figure 1A, B**). In contrast, 100-nm diameter liposomes diffused more slowly with
113 a diffusion time of 2.6 ± 0.2 ms, reflecting their larger size (**Figure 1C**). To allow labelled GP^{CL} to bind
114 liposomes under conditions that approximate the late endosome, GP^{CL} was incubated with liposomes
115 at 37°C for 20 mins at pH 5.5 across a range of Ca^{2+} concentrations. Evaluation with FCS indicated a
116 mixture of two species with diffusion times consistent with unbound GP^{CL}, and GP^{CL} bound to
117 liposomes. When liposomes were composed only of PC and cholesterol (PC:Ch 95:5) only 4.8 ± 0.1%
118 of GP^{CL} bound to liposomes in the absence of Ca^{2+} (**Figure 2**). With the addition of 1 μM Ca^{2+}, GP^{CL}
119 binding increased to 7.9 ± 0.2%. Increasing Ca^{2+} concentration as high as 1 mM did not further promote
120 GP^{CL} binding to the liposomes.

121 In contrast, when we introduced negatively charged PS into the liposomes (PC:PS:Ch 55:40:5), GP^{CL}
122 binding increased to 10.9 ± 0.2% in the absence of Ca^{2+}. Addition of Ca^{2+} at concentrations 1 μM and
123 10 μM further increased GP^{CL} binding to 17.9 ± 0.3% and 27.5 ± 0.2%, respectively. However, further
124 increases in Ca^{2+} concentration to 0.1 mM and 1 mM, reduced GP^{CL} binding by more than 1.3 and 4-
125 fold, respectively. Next, we evaluated the effect of BMP, a negatively charged lipid unique to late
126 endosomal membranes, on binding of GP^{CL} to liposomes (Bissig & Gruenberg, 2013; Hullin-Matsuda
127 et al., 2014). Liposomes designed to mimic the late endosome (PC:PS:BMP:Ch 40:40:15:5) (Bissig &
128 Gruenberg, 2013) bound 26.7 ± 0.2% of GP^{CL} in the absence of Ca^{2+}. Gradually increasing Ca^{2+}
129 promoted GP^{CL} binding to the liposomes, reaching a peak of 52.0 ± 0.3 % bound GP^{CL} at 1 mM Ca^{2+}.

130 These data demonstrate that anionic lipids, especially BMP, promote GP^{CL}-membrane interaction in a
131 Ca^{2+}-dependent manner.

132 Previous reports have shown that removal of the glycan cap and acidic pH are critical for trimeric GP
133 to bind target membranes and promote lipid mixing in the absence of BMP (Brecher et al., 2012; Das
134 et al., 2020). We therefore tested whether the presence of BMP affected the importance of glycan
135 cap removal or pH during membrane binding. At neutral pH, 8 ± 1.7% GPΔTM bound to BMP-
136 containing liposomes, with minimal increase in the presence of 1 mM Ca^{2+} (**Figure 3A**). At pH 5.5,
137 binding increased slightly to 18.3 ± 2%, with 1 mM Ca^{2+} promoting binding further. GP^{CL} bound
138 liposomes at neutral pH to a similarly modest extent as GPΔTM, irrespective of Ca^{2+}. Binding was
139 increased by acidic pH and Ca^{2+} to a greater extent than that seen for GPΔmuc, reasserting the
140 significance of glycan cap cleavage in membrane binding of GP (**Figure 3B**). Taken together, these
141 results demonstrate that neither anionic lipids nor Ca^{2+} are sufficient to promote GP-membrane
142 interactions at neutral pH. At acidic pH the combination of anionic lipids and Ca^{2+} facilitates robust
143 GP^{CL} engagement with the membrane.

144 ***Mutation of histidine residues in GP^{CL} have differential effects on membrane binding***

145 We next tested the pH sensing potential of histidine residues in GP1 and GP2. Residues H139, H154,
146 H197, H516 and H549 were selected. Residue H139 was selected since it is present in the NPC1-binding
147 site of GP1. Similarly, H154 is proximal to the NPC1-binding site and interacts with hydrophobic
148 residues in the fusion loop, potentially stabilizing the pre-fusion conformation (J. E. Lee et al., 2008).
149 H197 resides adjacent to the glycan cap cleavage site near the C-terminus of GP1. Finally, H516 and
150 H549 flank the fusion loop and have a functional role during lipid mixing *in vitro* (J. Lee et al., 2016).
151 H39 was not included in our analysis as its location near the N terminus of GP1 and the lack of
152 intramolecular interactions outside of its immediate proximity make it less likely to contribute to
153 mediating the global conformation of GP. The following pKa values for the selected histidine residues
154 were predicted by PropKa: 5.2 (H139), 5.2 (H154), 6.9 (H516) and 7.2 (H549), suggesting that the
155 protonation state of these residues may change under physiological conditions, which encouraged us
156 to experimentally test these residues as putative pH sensors (Olsson et al., 2011; Søndergaard et al.,
157 2011). The predicted pKa for H39 was 8.3, further deemphasizing this residue as a potential sensor of
158 physiological pH change. H197 is not present in the available GP structures and thus a predicted pKa
159 was not calculated. We next introduced alanine substitutions at positions 139, 154, 197, 516, and 549
160 in GP1 and GP2. The expression and structure of the mutant proteins was verified by western blot and
161 ELISA using KZ52, an antibody specific to the native tertiary structure of GP (**Figure S2**) (J. E. Lee et al.,
162 2008; Maruyama et al., 1999). GP-membrane interaction was evaluated using our FCS assay with

163 PC:PS:BMP:Ch liposomes since they yielded maximal binding of GP under the conditions tested. Of the
164 five His mutants evaluated, H139A, H154A and H516A bound liposomes at approximately 10% at
165 neutral pH, similarly to wild-type GP^{CL} (**Figure 3C-G**). However, these mutants did not show increased
166 membrane binding at acidic pH or in the presence of Ca^{2+}. These data suggest that H139, H154, and
167 H516 are critical to the pH-induced enhancement of GP-membrane interaction. In contrast, the H197A
168 mutant bound liposomes similarly to wild-type across all conditions tested, indicating that H197 does
169 not contribute to pH-induced membrane binding. H549A binding to liposomes remained similar to
170 wild-type at neutral pH, and at acidic pH in the absence of Ca^{2+}. However, the addition of Ca^{2+} induced
171 no additional membrane binding. This indicates that either Ca^{2+} does not bind to the H549A mutant,
172 or Ca^{2+} binding does not induce the effect on GP structure that promotes interaction with the
173 membrane. Furthermore, these data show that protonation of residues H197 and H549 is not
174 necessary for pH-enhanced membrane binding.

175 ***The putative Ca^{2+}-binding site is essential for interaction with the target membrane***

176 A previous study demonstrated that Ca^{2+} ions interact with conserved acidic residues (D522, E523,
177 E540 and E545) flanking the fusion loop, suggesting an important role for these residues in EBOV
178 fusion (Nathan et al., 2020). Here, we investigated whether these residues are similarly critical to
179 membrane binding in the context of trimeric GP^{CL}. Alanine substitutions were introduced at the
180 putative site of Ca^{2+} binding in the fusion loop. Protein expression and native conformation were
181 evaluated as above. The D522A and E540A mutants were well expressed and maintained native
182 antigenicity (**Figure S2**); E523A and E545A aggregated in solution and hence were not considered
183 further. The D522A mutant bound to PC:PS:BMP:Ch liposomes to a comparable extent as wild-type
184 GP^{CL} at neutral pH with or without Ca^{2+} (**Figure 3H**). Under acidic conditions binding was reduced (15
185 ± 2%) and addition of Ca^{2+} had no effect. In contrast, the membrane binding activity of E540A was
186 similar to wild-type at acidic pH in the absence of Ca^{2+} (30 ± 3%, **Figure 3I**). However, a reduction in
187 membrane binding (13 ± 3%) was observed in the presence of Ca^{2+}. These findings lend further support
188 for the idea that acidic residues flanking the fusion loop play a critical role in Ca^{2+}-mediated binding of
189 GP to the target membrane.

190 ***Conformational dynamics of wild-type GP^{CL} during membrane binding***

191 We first sought to better characterize the conformational equilibrium of GP^{CL} through smFRET imaging
192 at neutral pH in the absence of Ca^{2+}. We modified a previously established smFRET imaging assay that
193 reports on conformational changes in GP2 (**Figure 4A, B**). We used pseudoparticles with GP containing
194 the HRV3C cleavage site and a non-natural amino acid, *trans*-cyclooct-2-ene-L-lysine (TCO*) at
195 positions 501 and 610, which enabled labelling with Cy3- and Cy5-tetrazine. Advancements in single-

196 molecule detection allowed us to resolve additional FRET states beyond what had previously been
197 reported (Materials and Methods). Hidden Markov modelling (HMM) of the individual smFRET traces
198 indicated the existence of 4 states (0.24 ± 0.08, 0.49 ± 0.08, 0.72 ± 0.08, and 0.92 ± 0.08) (**Figure 4C,**
199 **S4A**). The 0.92-FRET state (high FRET), which is consistent with the pre-fusion conformation reflected
200 in structures of GP (J. E. Lee et al., 2008; Zhao et al., 2016), predominated with 41 ± 1% occupancy at
201 pH 7.5 in the absence of Ca^{2+} (**Figure 4D**). HMM analysis indicated spontaneous transitions among the
202 other three FRET states and enabled construction of transition density plots (TDPs), which display the
203 relative frequency of transitions between each FRET state (**Figure 4E**). The TDP indicates that most
204 transitions occur in and out of the 0.92-FRET state, and between the 0.72- and 0.42-FRET states.
205 Transitions to and from the 0.24-FRET state were comparatively rare. Acidification to pH 5.5 reduced
206 the occupancy of the pre-fusion conformation to 21 ± 2% and resulted in more frequent transitions in
207 and out of the 0.24-FRET state (**Figure 4F**). Addition of 1 mM Ca^{2+} led to a further 2-fold reduction in
208 pre-fusion occupancy to 13±2%, and further increase in transitions to and from the 0.24-FRET state
209 (**Figure 4G**). Structures of GP in the pre-fusion conformation depict the fusion loop in a hydrophobic
210 cleft in the neighbouring protomer within the trimer (J. E. Lee et al., 2008; Zhao et al., 2016). Given
211 the sites of fluorophore attachment, we hypothesized that the low-FRET states (0.24 and 0.49 FRET)
212 might reflect conformations in which the fusion loop was released from the hydrophobic cleft to
213 positions where it can engage the target membrane. We therefore incubated the labelled
214 pseudovirions with PC:PS:BMP:Ch liposomes at pH 5.5 in the presence of 1 mM Ca^{2+}, exactly as in our
215 FCS experiments that indicated robust membrane binding. Interaction with liposomes further
216 decreased occupancy in the pre-fusion conformation to 5 ± 2% and increased the 0.24-FRET state
217 occupancy to 62 ± 1%. Overall dynamics decreased drastically with remaining transitions occurring in
218 and out of the 0.24-FRET state (**Figure 4H**). Taken together, these data identify 0.24 FRET as indicating
219 a GP^{CL} conformation that is enriched at pH 5.5 and Ca^{2+}, and further stabilized by interaction with a
220 target membrane.

221 ***Conserved histidines mediate GP^{CL} conformation at acidic pH***

222 Having identified histidine residues that are critical to GP-membrane interaction, we next sought to
223 determine the role of these residues in mediating GP conformational changes using smFRET. Similar
224 to wild-type GP^{CL}, the pre-fusion conformation (0.92 FRET) was predominant for H139A at pH 7.5 with
225 an occupancy of 37 ± 1%. However, unlike wild-type GP^{CL} the pre-fusion conformation occupancy of
226 H139A was reduced only by about 30% at acidic pH (compared to 50% for wild-type) indicating a
227 reduced sensitivity to pH (**Figure 5A**). Nonetheless, transitions to intermediate- and low-FRET states
228 increased at acidic pH to a greater extent than wild-type, which correlates with the higher infectivity
229 (**Figure S1C**). This indicates a maintained ability of H139A to undergo conformational changes (**Figure**

230 **4F, 5B**) but perhaps a greater dependence on NPC1 binding, which follows exposure to acidic pH in
231 the endosome, for stabilization of functional conformations. The H154A mutant showed a more
232 pronounced phenotype where its conformational equilibrium was insensitive to acidification, with a
233 modest increase in transitions to low FRET (**Figure 5A, C**). While occupancy of the pre-fusion
234 conformation remained at approximately 25% at both pH values tested, predominant occupancy was
235 seen in the 0.49-FRET state (**Figure S4C**). Thus, while the H154A mutation destabilizes the pre-fusion
236 conformation, the lack of sensitivity to acidic pH prevented access to a conformation competent for
237 membrane binding. Taken together with the loss of infectivity of the H154A mutant (**Figure S1C**)
238 (Manicassamy et al., 2005), these data support the identification of H154 as a critical sensor of acidic
239 pH and mediator of GP conformation. Finally, consistent with H197 residing in an unstructured loop,
240 not clearly engaged in intramolecular interactions, the H197A mutation had minimal impact on GP
241 conformation or function as compared to wild-type at the pH tested (**Figure 5D, S1C, S4D**).

242 Two histidine residues in GP2, H516 and H549, had distinct effects on GP conformation. The H516A
243 mutation induced a loss of sensitivity to changes in pH (**Figure 5A, E**), consistent with the observed
244 dysfunction in membrane binding and lack of infectivity (**Figure S1C**). Similar to the H154A mutant, a
245 slight increase in dynamics was seen and increased occupancy in the 0.49-FRET state (**Figure S4E**),
246 further indicating that this conformation is not competent for membrane binding. These data support
247 H516 also being a critical pH sensor and mediator of GP conformation. In contrast, the H549A mutant
248 underwent significant destabilisation of the pre-fusion conformation upon exposure to acidic pH, as
249 well as an increase in dynamics (**Figure 5A, F, S4F**). This observation correlates with the maintenance
250 of membrane binding under acidic conditions (in the absence of Ca^{2+}) and the modest decrease in
251 infectivity (**Figure S1C**). Thus, these data suggest that, while H549 may sense changes in pH, it is not a
252 determinant of global GP conformation.

253 ***Modulation of GP conformation by Ca^{2+}-coordinating residues***

254 We next asked whether the coordination of Ca^{2+} impacts GP conformation as part of its role in enabling
255 membrane binding. The D522A mutant, which is defective in Ca^{2+} coordination, membrane binding,
256 and infectivity, demonstrated a conformational equilibrium similar to wild-type GP at neutral pH in
257 the absence of Ca^{2+} (**Figure 6A**) (Nathan et al., 2020). A slight increase in dynamics was observed as
258 compared to wild-type GP, suggestive of the mutation increasing mobility of the N terminus and fusion
259 loop (**Figure 6B**). Acidification destabilized the pre-fusion conformation, consistent with the D522A
260 mutation not affecting sensitivity to pH (**Figure S4G**). As expected, the addition of Ca^{2+} had no effect
261 on the stability of the pre-fusion conformation (**Figure 6A**). In contrast, the E540A mutation, which
262 maintains functionality in membrane binding in the absence of Ca^{2+}, showed a destabilized pre-fusion

263 conformation as compared to wild-type even at neutral pH, again suggestive of increased N terminus
264 and fusion loop mobility. Acidification had minimal effect on the conformational equilibrium, although
265 dynamics increased slightly. In particular, transitions in and out of the low-FRET state increased as
266 seen for wild-type GP (**Figure 6C**). The addition of Ca^{2+} led to stabilization of the 0.72-FRET state,
267 suggesting that adopting this conformation is not sufficient for membrane binding (**Figure S4H**). Taken
268 together, these data on the D522A and E540A mutants clarify that coordination of Ca^{2+} is not critical
269 for destabilizing the pre-fusion conformation. Rather, the importance of Ca^{2+} coordination likely
270 comes at a later stage during interaction with the target membrane.

271 ***Structural basis for pH-induced conformational changes***

272 Finally, we investigated the structural basis for pH-induced conformational changes in GP^{CL} using
273 molecular dynamics (MD) simulation. We focused our attention on H154 and H516 as our
274 experimental data implicated these residues in sensing changes in pH. We developed atomistic models
275 of GP^{CL} using available coordinates (Materials and Methods) (Bornholdt et al., 2016). In one model,
276 histidine side chains were deprotonated to probe electrostatic interactions that would predominate
277 at neutral pH. In an alternative model, histidine side chains were fully protonated to approximate the
278 conditions of the acidic late endosome (pH 5-5.5). In both cases, the models were solvated in explicit
279 water and charge-neutralized with ions. Following energy minimization and equilibration, we analysed
280 the local dynamics in the proximity of H154 and H516 in a 225-ns simulation. The H154 side chain is
281 engaged in electrostatic interactions with the side chain of E178, which contacts the receptor-binding
282 site via interaction with R85. At the same time, the backbone carbonyl of H154 interacts
283 electrostatically with the backbone amide N of Y534 in the fusion loop of the neighbouring protomer
284 (**Figure 7A**). H154 thus provides a linkage between the receptor-binding site and the fusion loop,
285 potentially stabilizing both regions in the pre-fusion conformation. According to our simulation,
286 protonation of H154 strengthens the interaction with E178, which pulls H154 away from Y534. This
287 movement destabilizes the H154-Y534 interaction, leading to greater relative movement of these
288 residues (**Figure 7B**). The simulation, therefore, suggests that protonation of H154 contributes to
289 release of the fusion loop from the hydrophobic cleft, facilitating its interaction with the target
290 membrane. Mutation of H154 would break the linkage with E178, enabling stable contact with Y534
291 across a range of pHs. The simulation thus provides a rationale for our experimental observation that
292 the GP2 conformation of the H154A mutant showed decreased sensitivity to acidic pH.

293 H516 flanks the fusion loop and is engaged in Pi-Pi stacking interaction with the side chain of W104 in
294 GP1. Here again, this interaction likely mediates the stability of the fusion loop in the pre-fusion
295 conformation. Our MD simulation suggests that this interaction is labile when H516 is deprotonated,

296 with H516 sampling multiple conformations (**Figure 7C, D**). These dynamics can be parameterized by
297 the distance between H516 and W104, and the χ_2 dihedral angle of the H516 side chain. Protonation
298 of H516 stabilized the stacking interaction with W104, reducing the dynamics of H516 and selecting a
299 single pre-existing conformation (**Figure 7E**). These data imply that GP1-GP2 interaction may be critical
300 to GP2 conformational changes that remove the fusion loop from the hydrophobic cleft. The H516-
301 W104 interaction may aid in ensuring proper positioning of the fusion loop for initial interaction with
302 the membrane. This would likely require that GP1 is repositioned in response to acidic pH. Mutation
303 of H516 may serve to decouple fusion loop release from putative GP1 movement.

304 **Discussion**

305 Previous studies indicate critical roles for acidic pH, Ca^{2+}, removal of the glycan cap, and NPC1 binding
306 during EBOV entry and GP-induced membrane fusion (Brecher et al., 2012; Carette et al., 2011; Côté
307 et al., 2011; Das et al., 2020; Gregory et al., 2011; Miller et al., 2012; Nathan et al., 2020; Sakurai et
308 al., 2015). However, live-cell imaging and cell-cell fusion experiments have demonstrated that
309 additional factors are necessary for completion of membrane fusion (Fénéant et al., 2019; Simmons
310 et al., 2016; Spence et al., 2016). In the present study, using a new developed FCS assay to quantify
311 the interactions between GP and liposomes, we show that endosomal anionic lipids, including PS and
312 BMP, promote Ca^{2+}-dependent membrane binding of GP^{CL} at acidic pH. Under the conditions tested,
313 membrane binding was optimal in the presence of both PS and BMP. It has been shown that Ca^{2+} binds
314 to PS in phospholipid bilayers and reduces its overall surface charge, which could explain the reduction
315 in binding of GP^{CL} with PC:PS:Ch liposomes at Ca^{2+} concentration higher than 10 µM in our
316 experimental setup (Martín-Molina et al., 2012; Melcrová et al., 2016). The additional presence of
317 BMP in liposomes drastically increased GP^{CL}-membrane binding. Additionally, unlike PC:PS:Ch
318 liposomes, increasing Ca^{2+} concentration did not limit interaction of GP^{CL} with PC:PS:BMP:Ch
319 liposomes. Rather, an increase in GP^{CL} binding was observed with increasing Ca^{2+} concentration with
320 maximal binding at 1 mM Ca^{2+}. Previous observations indicate that the unique structure of BMP alters
321 the negative spontaneous curvature of membranes (Matsuo et al., 2004). Additionally, BMP increases
322 the net surface charge of liposomes, enhancing their interaction with Ca^{2+} (Kobayashi et al., 2002).
323 Both features of BMP may promote efficient interaction between GP^{CL} and the target membrane. In
324 the latter case, GP^{CL} could preferentially interact with BMP via Ca^{2+} coordination within the fusion
325 loop. Since BMP is exclusively present in the late endosome (Kobayashi et al., 2002), it could also
326 regulate the timing of fusion of EBOV by avoiding pre-mature engagement of the fusion loop with a
327 membrane prior to arrival in the late endosome. A similar dependence on BMP has been reported for
328 other enveloped viruses such as Dengue virus, Lassa virus, vesicular stomatitis virus, and influenza
329 virus (Mannsverk et al., 2022; Markosyan et al., 2021; Matos et al., 2013; Zaitseva et al., 2010).

330 Whether downstream events during EBOV fusion are also accelerated by BMP, as reported for Lassa
331 virus, will be the topic of future studies (Markosyan et al., 2021).

332 The conformational changes in GP^{CL} under conditions favourable for membrane binding were
333 elucidated by a previously validated smFRET imaging assay developed in our lab, which reports on the
334 movement of the N-terminus of GP2 (Das et al., 2020). In the present work, we show that acidification
335 of pH followed by addition of Ca^{2+} leads to a sequential destabilization of the pre-fusion conformation
336 of GP^{CL}. An increase in low FRET under the same conditions suggests movement of the N terminus.
337 This change in FRET efficiency (ΔFRET = 0.68) equates to an increase in the distance between the
338 fluorophores of more than 30 Å. A movement of this magnitude likely also incorporates displacement
339 of the fusion loop away from the hydrophobic cleft to a position that is competent for membrane
340 binding. This interpretation is supported by our smFRET data acquired following incubation of GP^{CL}
341 with liposomes at acidic pH in the presence of Ca^{2+}, which led to further destabilization of the high-
342 FRET pre-fusion conformation, stabilization of the low-FRET conformation, and reduction of overall
343 kinetics (**Figure 4B, C**). A structural description of the low-FRET conformation will require additional
344 FRET pairs, which report more explicitly and with more sensitivity on the position of the fusion loop.
345 The hypothesized extended pre-hairpin intermediate in which the heptad repeat helix 1 (HR1) has
346 linearized may require repositioning or dissociation of GP1. Here again, additional FRET pairs that
347 report on inter-domain dynamics will be beneficial. Whatever the precise structural description of the
348 low-FRET state, our FCS and smFRET imaging results indicate that the extent of GP-membrane binding
349 is inversely correlated (Spearmen correlation r_S = -0.6813, p = 0.0127) with the occupancy of GP in the
350 pre-fusion conformation (**Figure 8**).

351 Protonation of amino acid side chains is the driving force for inducing conformational changes in viral
352 fusion proteins in response to acidification of pH. In particular, the role of histidine residues is well
353 established in triggering membrane binding and fusion of influenza virus, Semiliki Forest virus, and
354 human metapneumoviruses (Caffrey & Lavie, 2021; Harrison et al., 2013). Here, we report that
355 residues H139, H154, H516 and H549 tune the responsiveness of EBOV GP to acidic pH through both
356 stabilizing and destabilizing mechanisms. The membrane binding ability of H139A was reduced at
357 acidic pH accompanied by poor destabilization of the pre-fusion conformation relative to wild type,
358 indicating reduced ability to undergo pH-induced conformational changes in the absence of NPC1 *in*
359 *vitro*. Nonetheless, H139A maintained greater infectivity than wild-type. This may be due to greater
360 stability in the acidic endosome and given the proximity of H139 to the receptor-binding site, perhaps
361 higher affinity for NPC1 inside cells. Mutants H154A and H516A emerged as the most important pH
362 sensors. The membrane binding ability of both mutants was diminished at acidic pH and no difference
363 in their FRET occupancies at neutral or acidic pH was observed. This indicates that the mutants are

364 insensitive to changes in pH and thus, functionally inactive **(Figure 5C, E).** Histidine residues can
365 interact electrostatically with cationic amino acids such as lysine or arginine, forming His-Cat pairs,
366 which are known to stabilize the pre-fusion conformations of several viral envelope glycoproteins
367 (Harrison et al., 2013). These interactions are destabilized by protonation of histidines upon
368 acidification, leading to repulsion between histidines and cationic amino acid, which contribute to
369 triggering conformational changes necessary for viral fusion. In contrast, our MD simulation suggests
370 that H154 and H516 are engaged in interactions not described by the His-Cat paradigm. These data
371 indicate that protonation of H154 contributes to release of the fusion loop from its hydrophobic cleft
372 through a stabilized interaction with E178. According to our analysis, the strengthened H154-E178
373 interaction destabilizes backbone electrostatics between H154 and Y534 in the fusion loop of the
374 neighbouring protomer. Similarly, protonation of H516 stabilizes Pi-Pi stacking interaction with W104
375 in GP1. Thus, an inter-subunit interaction is strengthened under conditions that promote membrane
376 binding. This interaction may mediate positioning and stability of the fusion loop and may indicate
377 that GP1 remains associated with GP2 until after engagement with the target membrane. NPC1
378 binding to GP1 may partially serve to localize EBOV on the endosomal membrane to increase the
379 efficiency with which the fusion loop inserts into the membrane. At this point, an additional
380 endosomal factor may be required to enable transition to the post-fusion conformation, which
381 putatively requires dissociation of GP1.

382 Mutagenesis of H549 did not affect membrane binding or the extent of destabilization of the pre-
383 fusion conformation of GP at acidic pH, indicating that it is less critical for mediating changes in the
384 global conformation of GP. Additionally, membrane binding of H549A was insensitive to the presence
385 of Ca^{2+}. This could be due to H549A attaining a local conformation that is unresponsive to Ca^{2+}. These
386 results suggest that H549 more likely regulates the local conformation of the fusion loop, rather than
387 the release from the hydrophobic cleft. Taken together, our data indicate that acidic pH destabilizes
388 the interactions within GP1, and between GP1 and GP2 by direct side-chain protonation of key
389 histidine residues, similar to influenza HA1 and HA2 (Caffrey & Lavie, 2021; Harrison et al., 2013).

390 Ca^{2+} has been implicated in the fusion processes of Rubella virus, MERS-CoV, SARS-CoV-1 and -2, and
391 EBOV (Dubé et al., 2014; Lai et al., 2017; Nathan et al., 2020; Singh et al., 2022; Straus et al., 2020).
392 Ca^{2+} can assist in membrane fusion through coordination by anionic residues in the fusion loop, as first
393 seen for the Rubella virus E1 glycoprotein. This may stabilize a fusion loop conformation that is optimal
394 for insertion into the membrane. In addition, Ca^{2+} coordination in the fusion loop can affect the
395 physical properties of the target membrane in a manner that promotes fusion (Lai et al., 2017).
396 Previous studies have shown that compounds that lead to accumulation of Ca^{2+} in endosomes inhibit
397 EBOV entry, which indicates that EBOV fusion is highly sensitive to endosomal Ca^{2+} concentration (Das

398 et al., 2020; Johansen et al., 2013). *In vitro* studies have demonstrated that Ca^{2+} concentrations greater
399 than 500 µM are antagonistic to lipid mixing and fusion activity of Rubella virus, SARS-CoV-2, and EBOV
400 (Das et al., 2020; Dubé et al., 2014; Singh et al., 2022). A previous study of the isolated fusion loop of
401 EBOV GP highlighted the role of anionic residues, D522 and E540, in interaction with Ca^{2+} during
402 membrane binding and lipid mixing (Nathan et al., 2020). Our findings support these conclusions and
403 demonstrate that sensitivity of the native GP trimer to Ca^{2+}, and its ability to engage the target
404 membrane in the presence of Ca^{2+}, is mediated by residues D522 and E540. The mutant D522A
405 displayed destabilization of the pre-fusion conformation comparable to wild-type at acidic pH. Given
406 the loss of membrane binding by the D522A mutant, these data indicate that acidification of pH is the
407 major driver of global GP conformation, whereas Ca^{2+} binding may influence the local conformation
408 of the fusion loop, enabling optimal insertion into the membrane. On the contrary, there was no
409 significant change in the global conformation of E540A after acidification of pH. However, efficient
410 membrane binding of E540A at acidic pH, coupled with an increase in the frequency of transitions,
411 points toward a role for the target membrane in selecting conformations in E540A. Addition of Ca^{2+}
412 enriched the 0.72 FRET state, reduced both conformational transitions and membrane binding of
413 E540A. These data suggest that Ca^{2+} still binds the fusion loop of the E540A trimer in such a manner
414 that restricts the movement necessary for membrane binding. The NMR structure of the fusion loop
415 in DPC micelles at acidic pH shows a 90° bend, which reduces the distance between residues D522 and
416 H549, and between E540 and E545, bringing them within ~5 Å (Gregory et al., 2011). This could reflect
417 a conformation that becomes accessible to the fusion loop after transitioning out of the hydrophobic
418 cleft. The insensitivity of H549A to Ca^{2+} and its proximity to D522 at acidic pH in the NMR-derived
419 structure might suggest that this conformation is stabilized by Ca^{2+}, perhaps through coordination by
420 these pairs of residues. Structural studies of the intact trimer, performed under conditions that
421 promote membrane fusion, are needed to elucidate the global GP conformation and the local fusion
422 loop configuration that enables engagement with the target membrane. Biophysical interrogations
423 such as those presented here should guide these future studies by identifying conditions that promote
424 functional conformations and the residues that mediate their stability.

425 **Material and Methods**

426 ***Cell lines***

427 Expi293F cells (Gibco, ThermoFisher Scientific, Waltham, MA) were cultured in Expi293 expression
428 medium in an orbital shaking incubator at 37°C, 8% CO_2, 125rpm. HEK293T FirB cells, which have high
429 furin expression, were a kind gift from Dr. Theodore C. Pierson (Emerging Respiratory Virus section,
430 Laboratory of Infectious Diseases, NIH, Bethesda, MD) (Mukherjee et al., 2014). These cells were
431 cultured in DMEM (Gibco, ThermoFisher Scientific, Waltham, MA) with 10% cosmic calf serum

432 (Hyclone, Cytiva Life Sciences, Marlborough, MA) and 1% penicillin-streptomycin (Gibco,
433 ThermoFisher Scientific, Waltham, MA) at 37°C, 5% CO_2.

434 ***Plasmids***

435 pHLsec-GPΔTM and pMAM51-GPΔmuc plasmids were obtained from Dr. Kartik Chandran's lab
436 (Einstein College of Medicine, NY). pHLsec-GPΔTM encodes EBOV (Mayinga) GP sequence (UniProt
437 Q05320) with deleted mucin-like and transmembrane domains. A T4 fibritin foldon trimerization
438 domain and 6X-histidine tag for Ni-NTA purification has been inserted into the C terminus. The A1
439 (*GDSLDMLEWSLM*) and A4 (*DSLSMLEW*) peptides were introduced at positions 32 and 501 in GP1 and
440 GP2, respectively, for site-specific labelling of GPΔTM, as previously described (Durham et al., 2020).
441 pMAM51-GPΔmuc encodes full-length GP with the mucin-like domain deleted and was used for all
442 pseudovirion experiments. In both GPΔTM and GPΔmuc the thermolysin cleavage site, *VNAT* at
443 position 203, was replaced with an HRV3C protease recognition site (*LEVLFQGP*) by site directed
444 mutagenesis (Q5 site directed mutagenesis kit, New England Biolabs, Ipswich, MA). All amino acid
445 substitutions were also introduced in GPΔTM and GPΔmuc via site-directed mutagenesis.
446 pNL4.3.Luc.R-E- used in infectivity assays was obtained through the NIH AIDS Reagent program
447 (contributed by Dr. Nathaniel Landau, New York University School of Medicine) (He et al., 1995). An
448 amber stop codon (TAG) in the *tat* gene was modified by site-directed mutagenesis to --TAA to prevent
449 readthrough during incorporation of TCO* for labelling of GPΔmuc. Plasmids $PyIRS^{AF}$ and eRF1 were
450 provided by Dr. Edward Lemke (Johannes Gutenberg-University of Mainz, Germany).

451 ***Protein expression and purification***

452 For production of GPΔTM proteins (wild-type and mutants), Expi293F cells were transfected with
453 pHLsec-GPΔTM using polyethyleneimine (PEI MAX, Polysciences, Warrington, PA) at a mass ratio of
454 1:3 DNA:PEI MAX. As previously described, a 2:1 ratio of pHLsec-GPΔTM to tagged pHLsec-GPΔTM was
455 transfected to ensure that GPΔTM trimers contained on average a single tagged protomer. The
456 supernatants containing soluble GPΔTM proteins were harvested 5 days post-transfection. The
457 proteins were purified using Ni-NTA agarose beads (Pierce, ThermoFisher Scientific, Waltham, MA).
458 The protein was bound to the column in phosphate-buffered saline (PBS) containing 10mM imidazole,
459 followed by washing with 20mM imidazole in PBS and elution in 200 mM imidazole containing PBS.
460 Following purification, proteins were exchanged to labelling buffer (20 mM HEPES, 50 mM NaCl, pH
461 7.5) using VivaSpin 6 concentrator (Sartorius AG, Gottingen, Germany).

462 ***Labelling of GPΔTM***

463 Wild-type and mutant GPΔTM proteins were labelled with 5 µM LD650 conjugated to coenzyme A
464 (LD650-CoA; Lumidyne Technologies, New York, NY). The fluorophore was attached to the A1 and A4

465 peptides in the tagged GPΔTM through incubation with 5 µM acyl carrier protein synthase (AcpS) in
466 the labelling buffer with 10 mM $Mg(CH_3COO)_2$ overnight at room temperature (Durham et al., 2020).
467 The labelled proteins were subjected to overnight cleavage by exogenous furin (New England Biolabs,
468 Ipswich, MA) at 37°C to fully convert GP0 to GP1 and GP2. The processed proteins were purified by
469 size-exclusion chromatography on a Superdex 200 Increase 10/300 GL column (GE Healthcare,
470 Chicago, IL). Purified, labelled proteins were concentrated using Amicon Ultra 30K filters
471 (MilliporeSigma, Burlington, MA), aliquoted and stored at -80°C until further use. The concentration
472 of proteins was determined using Bradford reagent.

473 ***Indirect ELISA***

474 Labelled proteins were diluted to a final concentration of 5 µg/ml in PBS and coated onto the wells of
475 a 96-well polystyrene plate (Pierce™, ThermoFisher Scientific, Waltham, MA) by incubating overnight
476 at 4°C. The plate was washed three times with PBST (PBS with 0.1% Tween-20) followed by blocking
477 with 5% skim milk in PBST for 3h at room temperature. The blocking solution was removed, and the
478 plate was again washed twice with PBST. Proteins were probed with KZ52 antibody (Durham et al.,
479 2020; Maruyama et al., 1999) at a dilution of 1:1000 overnight at 4°C. The plate was then washed and
480 incubated with horseradish peroxidase-conjugated anti-human IgG (Invitrogen™, ThermoFisher
481 Scientific, Waltham, MA) at a dilution of 1:2000 for 2h at room temperature. After washing the plate
482 four times with PBST, TMB solution (3,3',5,5'-tetramethylbenzidine; ThermoFisher Scientific,
483 Waltham, MA) was added to each well, incubated for 15 min, followed by addition of an equal volume
484 of 2M sulphuric acid. The optical density was immediately read at 450 nm in a Synergy H1 microplate
485 reader (BioTek, Winooski, VT).

486 ***Liposome preparation***

487 The following lipids were used for liposome preparation: POPC (1-palmitoyl-2-oleoyl-glycero-3-
488 phosphocholine), POPS (1-palmitoyl-2-oleoyl-sn-glycero-3-phospho-L-serine (sodium salt)), BMP
489 (bis(monooleoylglycero)phosphate (S,R Isomer)) and cholesterol (all from Avanti Polar lipids,
490 Alabaster, AL). Stock solution of lipids (10 mg/ml) were diluted at desired ratios in chloroform to obtain
491 a final total lipid concentration of 1 mM. A lipid film was formed in a glass vial by evaporating the
492 chloroform under a steady stream of Argon gas. Residual chloroform was removed by incubating the
493 lipid film overnight under vacuum. Lipids were rehydrated with 5 mM HEPES, 10 mM MES and 150
494 mM NaCl, pH 7.5, for 1 hour at room temperature. The lipid suspension was vortexed 5-7 times in 10
495 sec pulses followed by 10 freeze-thaw cycles with liquid nitrogen. Liposomes were formed by
496 extruding the lipid solution 37 times through a 100 nm polycarbonate membrane (Whatman®
497 Nucleopore™ track-etched membrane) in a mini-extruder (Avanti Polar Lipids, Alabaster, AL). The size

498 of liposomes was verified using dynamic light scattering (Zetasizer Nano, Malvern Panalytical,
499 Malvern, UK). The liposomes were stored at 4°C and used within a week.

500 ***HRV3C cleavage***

501 The glycan cap was removed from GPΔTM and pseudovirions with GPΔmuc through incubation with
502 HRV3C protease (Pierce™, ThermoFisher Scientific, Waltham, MA) at 10°C for 16 hr. Cleavage of
503 LD650-labelled GPΔTM was verified by in-gel fluorescence imaging of uncleaved and cleaved protein
504 on a 4-20% polyacrylamide using a ChemiDoc™ MP imaging system (Bio-Rad, Hercules, CA) followed
505 by Coomassie staining.

506 ***Fluorescence correlation spectroscopy***

507 For membrane binding studies, liposomes (500 µM total lipid) were incubated with 5 nM labelled
508 GPΔTM in 5 mM HEPES, 10 mM MES, 150 mM NaCl (pH 7.5 or 5.5). For experiments performed in the
509 absence of Ca^{2+}, 1mM EDTA was included to chelate any Ca^{2+} already bound to GPΔTM. Otherwise,
510 the indicated concentration of $CaCl_2$ (0-1mM) was included in the incubation. The liposome-GPΔTM
511 mixture was incubated at 37°C for 20 min to allow binding. For experiments performed at pH 5.5, the
512 liposome mixture was acidified with 1 M HCl prior to addition of GPΔTM. FCS experiments were
513 performed by dropping 50 µL of the liposome-GPΔTM mixture onto a coverslip (No. 1.5 Thorlabs,
514 Newton, NJ). To prevent sticking of the protein-membrane complex to the glass surface, coverslips
515 were plasma-cleaned followed by coating with 10% polyethylene glycol (PEG-8000, Promega,
516 Madison, WI). 100 autocorrelation curves, 5 sec each in length, were recorded at room temperature
517 using a 638 nm laser in a CorTector SX100 (LightEdge Technologies Ltd., Zhongshan City, China). The
518 curves were fitted to the following model for two species diffusing in three dimensions with triplet
519 blinking (Betaneli et al., 2019; Ducas & Rhoades, 2012; Rhoades et al., 2006):

520 $G(\tau) = G_{triplet}(\tau).\, G_{complex}(\tau)$, where

521 $G_{triplet}(\tau) = 1 - T + T \cdot e^{\frac{\tau}{\tau_{triplet}}}$, and

522 $$G_{complex}(\tau) = \frac{1}{N}\left(f \cdot \left[1 + \frac{\tau}{\tau_{protein}}\right]^{-1} \left[1 + \frac{\tau}{s^2 \tau_{protein}}\right]^{-1/2} + \alpha \cdot (1 - f)\right.$$

523 $$\left. \cdot \left[1 + \frac{\tau}{\tau_{liposome}}\right]^{-1} \left[1 + \frac{\tau}{s^2 \tau_{liposome}}\right]^{-1/2} \right)$$

524

525 where, N is the number of molecules in the confocal volume, f is the fraction of free protein, α is the
526 average brightness of the protein-liposome complex, $\tau_{protein}$ is the diffusion time of free protein,
527 $\tau_{liposome}$ is the diffusion time of the liposome, and s is the structural parameter, which reflects the

528 dimensions of the confocal volume. The diffusion times, $\tau_{protein}$ and $\tau_{liposome}$ were calculated by
529 fitting the autocorrelation curves of GPΔTM and liposomes (labelled with DiD) separately to single
530 species diffusion models. The values of s and $\tau_{protein}$ were kept constant to calculate the fraction of
531 free and bound protein for all samples. Due to polydispersity of liposomes and fast photophysical
532 dynamics of triplet blinking, $\tau_{liposome}$ and $\tau_{triplet}$ were allowed to vary during fitting. The analysis was
533 carried out in MATLAB (MathWorks, Natick, MA) using a non-linear least-square curve fitting
534 algorithm. All values were averaged over three independent experiments.

535 ***Western blotting***

536 All proteins and pseudovirions were run on 4-20% denaturing polyacrylamide gels (Bio-Rad, Hercules,
537 CA) and transferred to nitrocellulose membrane using Trans-blot Turbo (Bio-Rad, Hercules, CA).
538 Membranes were rinsed with PBST, blocked with 5% skim milk in PBST for 1 h followed by probing of
539 GP and p24 with monoclonal antibody (mAb) H3C8 at a dilution of 1:1000, (Ou et al., 2010) and mouse
540 mAB B1217M at a dilution of 1:2000 (Genetex, Irvine, CA), respectively. The mAb H3C8 was humanized
541 by cloning its variable heavy and light chain fragments in human IgG expression vectors obtained from
542 Dr. Michel Nussenzwieg (The Rockefeller University). Membranes were washed three times with PBST,
543 incubated with horseradish peroxidase-conjugated anti-human IgG (Invitrogen™, ThermoFisher,
544 Waltham, MA) and anti-mouse IgG (ThermoFisher, Waltham, MA) for 1 h at room temperature and
545 developed with SuperSignal™ West Pico PLUS chemiluminescent substrate (ThermoFisher Scientific,
546 Waltham, MA).

547 ***Infectivity assay***

548 Infectivity of VSV pseudovirions containing wild-type GPΔmuc was compared to pseudovirions
549 containing GPΔmuc^{HRV3C} via flow cytometry (Whitt, 2010). HEK293T cells were transfected with
550 GPΔmuc and GPΔmuc^{HRV3C} plasmid using polyethyleneimine (PEI MAX, Polysciences, Warrington, PA)
551 at a mass ratio of 1:3 PEI MAX:DNA. Cells were transduced with VSVΔG-GFP-VSVG pseudovirions 24 h
552 after transfection. Supernatants containing VSVΔG-GFP-GPΔmuc and VSVΔG-GFP-GPΔmuc^{HRV3C} were
553 collected 24 h post-transduction and filtered through 0.45 µm filter. As a negative control, bald
554 particles were generated by transducing cells not expressing GPΔmuc. Vero cells were infected with
555 VSV pseudovirions through incubation at 37°C for 1 h with gentle agitation every 15min to allow even
556 spread of pseudovirions. Fresh media was added, and infection was allowed to proceed for five more
557 hours. Cells were trypsinized and assayed for expression of GFP using a flow cytometer (MACSQuant
558 Analyzer 1.0). The results were averaged across technical replicates and standard error was calculated
559 from biological replicates.

560 To assess infectivity of GPΔmuc^{HRV3C} mutants, pseudovirions with luciferase-expressing HIV-1 core
561 were produced. Plasmids pMAM51-GPΔmuc^{HRV3C} and pNL4.3.Luc.R-E- were co-transfected at a ratio
562 of 1:5 in HEK 293T FirB cells. Pseudovirions were harvested 24 h post-transfection by collecting the
563 supernatant, passing through a 0.45 µm filter, and layering on 10% sucrose in PBS solution followed
564 by ultracentrifugation at 25000 rpm for 2 h at 4°C. After resuspension of the pellet in PBS, particles
565 were analyzed by western blot. The virions were cleaved with HRV3C to remove the glycan cap as
566 above, incubated with Vero cells for 5 h at 37°C, followed by replacement of growth media. After 48
567 h, cells were lysed with Glo Lysis Buffer (Promega, Madison, WI) for 5 min at room temperature.
568 Luciferase activity was recorded by mixing equal volumes of cell lysate and Steady Glo Reagent
569 (Promega, Madison, WI) and reading in a Synergy H1 plate reader (Biotek, Winooski, VT). The
570 luminescence was normalized to expression of GP for each sample. Bald pseudovirions containing only
571 pNL4.3.Luc.R-E- were used as a negative control.

572 ***Pseudovirion production and labelling for smFRET imaging***

573 To facilitate attachment of fluorophores to GP on the surface of pseudovirions for smFRET imaging,
574 the non-natural amino acid TCO* (SiChem GmbH, Bremen, Germany) was introduced at positions 501
575 and 610 through amber stop codon suppression (GP*) (**Figure 4B**) (Nikić et al., 2016). Pseudovirions
576 were produced by transfecting HEK293T FirB cells with pMAM51-GPΔmuc^{HRV3C} plasmids with and
577 without amber stop codons at a 1:1 ratio, which equated to an excess of GP protein over GP*. This
578 ratio was optimized to ensure that the pseudovirions rarely contained more than a single GP*
579 protomer per particle. A plasmid encoding HIV-1 GagPol was also transfected to provide the
580 pseudovirion core. To increase the efficiency of amber codon readthrough, plasmids eRF1 and PyIRS^{AF}
581 were also included in transfection (Das et al., 2020; Nikić et al., 2016). The supernatant containing
582 pseudovirions was harvested 48 h post-transfection, filtered through a 0.45 µm mixed cellulose ester
583 membrane and layered onto 10% sucrose (in PBS) solution. The pseudovirions were pelleted by
584 ultracentrifugation at 25000 rpm for 2 h at 4°C. Pseudovirions were resuspended in 500 µL PBS and
585 incubated with 500 nM Cy3- and Cy5-tetrazine (Jena Biosciences, Jena, Germany) for 30 min at room
586 temperature. 60 µM DSPE-PEG2000 biotin (Avanti Polar Lipids, Alabaster, AL) was added to the
587 labelling reaction and incubated for another 30 min at room temperature with gentle mixing. The
588 labelling reaction was layered on a 6-30% OptiPrep (Sigma-Aldrich, MilliporeSigma, Burlington, MA)
589 density gradient and ultracentrifuged at 35000 rpm for 1 h at 4°C. Labelled pseudovirions were
590 collected, aliquoted, and analyzed by western blot.

591 ***smFRET imaging assay and data analysis***

592 All smFRET experiments were performed following removal of the glycan cap from GP. Labelled and
593 glycan cap-cleaved pseudovirions were immobilized on streptavidin-coated quartz slides and imaged
594 on a wide-field prism-based TIRF microscope (Blakemore et al., 2021). Imaging was performed in the
595 same buffer used for the membrane binding assay (5 mM HEPES, 10 mM MES, 150 mM NaCl [pH 7.5
596 or 5.5]). To study the effect of Ca^{2+}, the buffer was supplemented with 1 mM $CaCl_2$. smFRET data was
597 acquired at room temperature at 25 frames/sec using the MicroManager microscope control software
598 (micromanager.org). Analysis of smFRET data was performed using the SPARTAN software package
599 (https://www.scottcblanchardlab.com/software) (Juette et al., 2016) in MATLAB (MathWorks, Natick,
600 MA). smFRET trajectories were selected according to the following criteria: acceptor fluorescence
601 intensity greater than 35; FRET was detectable for at least 15 frames prior to photobleaching;
602 correlation coefficient between donor and acceptor fluorescence traces was less than -0.4; signal-to-
603 noise ratio was greater than 10; and background fluorescence was less than 50. Trajectories that met
604 these criteria were further verified manually and fitted to a 5-state linear hidden Markov model
605 (including a zero-FRET state) using maximum point likelihood (MPL) algorithm implemented in
606 SPARTAN (Qin et al., 2000). The 5-state linear model was chosen based on the Akaike Information
607 Criterium (AIC) and the Bayesian Inference Criterium (BIC) (**Figure S3**) (Akaike, 1974; Schwarz, 1978).
608 Several models were initially considered with varying numbers of model parameters and topology.
609 The 5-state linear model minimized both the AIC and BIC criteria relative to the models considered
610 and was thus chosen for analysis. The idealizations from total number of traces for each sample were
611 used to calculate the occupancies in different FRET states and construct the FRET histograms and
612 transition density plots (TDPs).

613 **MD simulation**

614 A model of trimeric GP^{CL} was generated from atomic coordinates determined through x-ray
615 crystallography (PDB accession: 5JQ3) (Zhao et al., 2016). Models included residues 32-188 of GP1 and
616 502-598 of GP2. Missing atoms, including hydrogens were added using pdb4amber. The protein
617 components of the models were parameterized with the Amber forcefield (ff14SB). The systems were
618 charge neutralized and solvated with the TIP3P explicit solvent model in LEaP. The solvated proteins
619 were energy minimized for 0.1 ns, followed by equilibration using a stepwise protocol (Shi et al., 2008).
620 Briefly, the protein backbone was harmonically constrained, with the constraints being released
621 stepwise over 4 0.3-ns intervals. The simulations were then run for 225 ns in the NPT ensemble.
622 Temperature and pressure were maintained using the Langevin thermostat and the Nose-Hoover
623 Langevin barostat, respectively. Electrostatics were calculated using the Particle Mesh Ewald
624 algorithm. All simulation steps were run using NAMD version 2.14 on the c3ddb cluster at the
625 Massachusetts Green High Performance Computing Center.

Acknowledgments

The authors would like to thank Dr. Marco Díaz-Salinas (UMass Chan Medical School, Worcester, MA) for creating substitution mutations in *tat* in pNL4.3.Luc.R-E- plasmid used in the present study. We would also like to thank Dr. Gang Han (UMass Chan Medical School, Worcester, MA) for providing the facility of dynamic light scattering. This work was supported by NIH grants R01AI174645 and R01GM143773 to J.B.M, and R01AI148784 to J.L.

References

Akaike, H. (1974). A new look at the statistical model identification. *IEEE Transactions on Automatic Control*, *19*(6), 716–723. https://doi.org/10.1109/tac.1974.1100705

Betaneli, V., Mücksch, J. & Schwille, P. (2019). Lipid-Protein Interactions, Methods and Protocols. *Methods in Molecular Biology*, *2003*, 415–447. https://doi.org/10.1007/978-1-4939-9512-7_18

Bissig, C. & Gruenberg, J. (2013). Lipid Sorting and Multivesicular Endosome Biogenesis. *Cold Spring Harbor Perspectives in Biology*, *5*(10), a016816. https://doi.org/10.1101/cshperspect.a016816

Bitto, D., Halldorsson, S., Caputo, A. & Huiskonen, J. T. (2016). Low pH and Anionic Lipid-dependent Fusion of Uukuniemi Phlebovirus to Liposomes*. *Journal of Biological Chemistry*, *291*(12), 6412–6422. https://doi.org/10.1074/jbc.m115.691113

Blakemore, R. J., Burnett, C., Swanson, C., Kharytonchyk, S., Telesnitsky, A. & Munro, J. B. (2021). Stability and conformation of the dimeric HIV-1 genomic RNA 5'UTR. *Biophysical Journal*, *120*(21), 4874–4890. https://doi.org/10.1016/j.bpj.2021.09.017

Bornholdt, Z. A., Ndungo, E., Fusco, M. L., Bale, S., Flyak, A. I., Crowe, J. E., Chandran, K. & Saphire, E. O. (2016). Host-Primed Ebola Virus GP Exposes a Hydrophobic NPC1 Receptor-Binding Pocket, Revealing a Target for Broadly Neutralizing Antibodies. *MBio*, *7*(1), e02154-15. https://doi.org/10.1128/mbio.02154-15

Brecher, M., Schornberg, K. L., Delos, S. E., Fusco, M. L., Saphire, E. O. & White, J. M. (2012). Cathepsin Cleavage Potentiates the Ebola Virus Glycoprotein To Undergo a Subsequent Fusion-Relevant Conformational Change. *Journal of Virology*, *86*(1), 364–372. https://doi.org/10.1128/jvi.05708-11

Caffrey, M. & Lavie, A. (2021). pH-Dependent Mechanisms of Influenza Infection Mediated by Hemagglutinin. *Frontiers in Molecular Biosciences*, *8*, 777095. https://doi.org/10.3389/fmolb.2021.777095

Carette, J. E., Raaben, M., Wong, A. C., Herbert, A. S., Obernosterer, G., Mulherkar, N., Kuehne, A. I., Kranzusch, P. J., Griffin, A. M., Ruthel, G., Cin, P. D., Dye, J. M., Whelan, S. P., Chandran, K. & Brummelkamp, T. R. (2011). Ebola virus entry requires the cholesterol transporter Niemann-Pick C1. *Nature*, *477*(7364), 340–343. https://doi.org/10.1038/nature10348

Chandran, K., Sullivan, N. J., Felbor, U., Whelan, S. P. & Cunningham, J. M. (2005). Endosomal Proteolysis of the Ebola Virus Glycoprotein Is Necessary for Infection. *Science*, *308*(5728), 1643–1645. https://doi.org/10.1126/science.1110656

663 Côté, M., Misasi, J., Ren, T., Bruchez, A., Lee, K., Filone, C. M., Hensley, L., Li, Q., Ory, D., Chandran, K.
664 & Cunningham, J. (2011). Small molecule inhibitors reveal Niemann–Pick C1 is essential for Ebola
665 virus infection. *Nature*, *477*(7364), 344–348. https://doi.org/10.1038/nature10380

666 Das, D. K., Bulow, U., Diehl, W. E., Durham, N. D., Senjobe, F., Chandran, K., Luban, J. & Munro, J. B.
667 (2020). Conformational changes in the Ebola virus membrane fusion machine induced by pH,
668 Ca2+, and receptor binding. *PLoS Biology*, *18*(2), e3000626.
669 https://doi.org/10.1371/journal.pbio.3000626

670 Diseases, T. L. I. (2022). Ebola returns: back to square one. *The Lancet Infectious Diseases*.
671 https://doi.org/10.1016/s1473-3099(22)00678-8

672 Dubé, M., Rey, F. A. & Kielian, M. (2014). Rubella Virus: First Calcium-Requiring Viral Fusion Protein.
673 *PLoS Pathogens*, *10*(12), e1004530. https://doi.org/10.1371/journal.ppat.1004530

674 Ducas, V. C. & Rhoades, E. (2012). Quantifying Interactions of β-Synuclein and γ-Synuclein with
675 Model Membranes. *Journal of Molecular Biology*, *423*(4), 528–539.
676 https://doi.org/10.1016/j.jmb.2012.08.008

677 Durham, N. D., Howard, A. R., Govindan, R., Senjobe, F., Fels, J. M., Diehl, W. E., Luban, J., Chandran,
678 K. & Munro, J. B. (2020). Real-Time Analysis of Individual Ebola Virus Glycoproteins Reveals Pre-
679 Fusion, Entry-Relevant Conformational Dynamics. *Viruses*, *12*(1), 103.
680 https://doi.org/10.3390/v12010103

681 Fénéant, L., Wijs, K. M. S., Nelson, E. A. & White, J. M. (2019). An exploration of conditions proposed
682 to trigger the Ebola virus glycoprotein for fusion. *PLoS ONE*, *14*(7), e0219312.
683 https://doi.org/10.1371/journal.pone.0219312

684 Gregory, S. M., Harada, E., Liang, B., Delos, S. E., White, J. M. & Tamm, L. K. (2011). Structure and
685 function of the complete internal fusion loop from Ebolavirus glycoprotein 2. *Proceedings of the*
686 *National Academy of Sciences*, *108*(27), 11211–11216. https://doi.org/10.1073/pnas.1104760108

687 Harrison, J. S., Higgins, C. D., O'Meara, M. J., Koellhoffer, J. F., Kuhlman, B. A. & Lai, J. R. (2013). Role
688 of Electrostatic Repulsion in Controlling pH-Dependent Conformational Changes of Viral Fusion
689 Proteins. *Structure*, *21*(7), 1085–1096. https://doi.org/10.1016/j.str.2013.05.009

690 He, J., Choe, S., Walker, R., Marzio, P. D., Morgan, D. O. & Landau, N. R. (1995). Human
691 immunodeficiency virus type 1 viral protein R (Vpr) arrests cells in the G2 phase of the cell cycle
692 by inhibiting p34cdc2 activity. *Journal of Virology*, *69*(11), 6705–6711.
693 https://doi.org/10.1128/jvi.69.11.6705-6711.1995

694 Hullin-Matsuda, F., Taguchi, T., Greimel, P. & Kobayashi, T. (2014). Lipid compartmentalization in the
695 endosome system. *Seminars in Cell & Developmental Biology*, *31*, 48–56.
696 https://doi.org/10.1016/j.semcdb.2014.04.010

697 Johansen, L. M., Brannan, J. M., Delos, S. E., Shoemaker, C. J., Stossel, A., Lear, C., Hoffstrom, B. G.,
698 DeWald, L. E., Schornberg, K. L., Scully, C., Lehár, J., Hensley, L. E., White, J. M. & Olinger, G. G.
699 (2013). FDA-Approved Selective Estrogen Receptor Modulators Inhibit Ebola Virus Infection.
700 *Science Translational Medicine*, *5*(190), 190ra79. https://doi.org/10.1126/scitranslmed.3005471

701 Juette, M. F., Terry, D. S., Wasserman, M. R., Altman, R. B., Zhou, Z., Zhao, H. & Blanchard, S. C.
702 (2016). Single-molecule imaging of non-equilibrium molecular ensembles on the millisecond
703 timescale. *Nature Methods*, *13*(4), 341–344. https://doi.org/10.1038/nmeth.3769

704 Kobayashi, T., Beuchat, M.-H., Chevallier, J., Makino, A., Mayran, N., Escola, J.-M., Lebrand, C.,
705 Cosson, P., Kobayashi, T. & Gruenberg, J. (2002). Separation and Characterization of Late
706 Endosomal Membrane Domains*. *Journal of Biological Chemistry*, *277*(35), 32157–32164.
707 https://doi.org/10.1074/jbc.m202838200

708 Lai, A. L., Millet, J. K., Daniel, S., Freed, J. H. & Whittaker, G. R. (2017). The SARS-CoV Fusion Peptide
709 Forms an Extended Bipartite Fusion Platform that Perturbs Membrane Order in a Calcium-
710 Dependent Manner. *Journal of Molecular Biology*, *429*(24), 3875–3892.
711 https://doi.org/10.1016/j.jmb.2017.10.017

712 Lee, J. E., Fusco, M. L., Hessell, A. J., Oswald, W. B., Burton, D. R. & Saphire, E. O. (2008). Structure of
713 the Ebola virus glycoprotein bound to an antibody from a human survivor. *Nature*, *454*(7201),
714 177–182. https://doi.org/10.1038/nature07082

715 Lee, J., Gregory, S. M., Nelson, E. A., White, J. M. & Tamm, L. K. (2016). The Roles of Histidines and
716 Charged Residues as Potential Triggers of a Conformational Change in the Fusion Loop of Ebola
717 Virus Glycoprotein. *PLoS ONE*, *11*(3), e0152527. https://doi.org/10.1371/journal.pone.0152527

718 Manicassamy, B., Wang, J., Jiang, H. & Rong, L. (2005). Comprehensive Analysis of Ebola Virus GP1 in
719 Viral Entry. *Journal of Virology*, *79*(8), 4793–4805. https://doi.org/10.1128/jvi.79.8.4793-
720 4805.2005

721 Mannsverk, S., Giraldo, A. M. V. & Kasson, P. M. (2022). Influenza Virus Membrane Fusion Is
722 Promoted by the Endosome-Resident Phospholipid Bis(monoacylglycero)phosphate. *The Journal*
723 *of Physical Chemistry. B*, *126*(49), 10445–10451. https://doi.org/10.1021/acs.jpcb.2c06642

724 Markosyan, R. M., Marin, M., Zhang, Y., Cohen, F. S. & Melikyan, G. B. (2021). The late endosome-
725 resident lipid bis(monoacylglycero)phosphate is a cofactor for Lassa virus fusion. *PLoS Pathogens*,
726 *17*(9), e1009488. https://doi.org/10.1371/journal.ppat.1009488

727 Martín-Molina, A., Rodríguez-Beas, C. & Faraudo, J. (2012). Effect of calcium and magnesium on
728 phosphatidylserine membranes: experiments and all-atomic simulations. *Biophysical Journal*,
729 *102*(9), 2095–2103. https://doi.org/10.1016/j.bpj.2012.03.009

730 Maruyama, T., Rodriguez, L. L., Jahrling, P. B., Sanchez, A., Khan, A. S., Nichol, S. T., Peters, C. J.,
731 Parren, P. W. H. I. & Burton, D. R. (1999). Ebola Virus Can Be Effectively Neutralized by Antibody
732 Produced in Natural Human Infection. *Journal of Virology*, *73*(7), 6024–6030.
733 https://doi.org/10.1128/jvi.73.7.6024-6030.1999

734 Matos, P. M., Marin, M., Ahn, B., Lam, W., Santos, N. C. & Melikyan, G. B. (2013). Anionic lipids are
735 required for vesicular stomatitis virus G protein-mediated single particle fusion with supported
736 lipid bilayers. *The Journal of Biological Chemistry*, *288*(18), 12416–12425.
737 https://doi.org/10.1074/jbc.m113.462028

738 Matsuo, H., Chevallier, J., Mayran, N., Blanc, I. L., Ferguson, C., Fauré, J., Blanc, N. S., Matile, S.,
739 Dubochet, J., Sadoul, R., Parton, R. G., Vilbois, F. & Gruenberg, J. (2004). Role of LBPA and Alix in

740 Multivesicular Liposome Formation and Endosome Organization. *Science*, *303*(5657), 531–534.
741 https://doi.org/10.1126/science.1092425

742 Mazzon, M. & Mercer, J. (2014). Lipid interactions during virus entry and infection. *Cellular*
743 *Microbiology*, *16*(10), 1493–1502. https://doi.org/10.1111/cmi.12340

744 Melcrová, A., Pokorna, S., Pullanchery, S., Kohagen, M., Jurkiewicz, P., Hof, M., Jungwirth, P., Cremer,
745 P. S. & Cwiklik, L. (2016). The complex nature of calcium cation interactions with phospholipid
746 bilayers. *Scientific Reports*, *6*(1), 38035. https://doi.org/10.1038/srep38035

747 Miller, E. H., Obernosterer, G., Raaben, M., Herbert, A. S., Deffieu, M. S., Krishnan, A., Ndungo, E.,
748 Sandesara, R. G., Carette, J. E., Kuehne, A. I., Ruthel, G., Pfeffer, S. R., Dye, J. M., Whelan, S. P.,
749 Brummelkamp, T. R. & Chandran, K. (2012). Ebola virus entry requires the host-programmed
750 recognition of an intracellular receptor. *The EMBO Journal*, *31*(8), 1947–1960.
751 https://doi.org/10.1038/emboj.2012.53

752 Mukherjee, S., Dowd, K. A., Manhart, C. J., Ledgerwood, J. E., Durbin, A. P., Whitehead, S. S. &
753 Pierson, T. C. (2014). Mechanism and significance of cell type-dependent neutralization of
754 flaviviruses. *Journal of Virology*, *88*(13), 7210–7220. https://doi.org/10.1128/jvi.03690-13

755 Mulherkar, N., Raaben, M., Torre, J. C. de la, Whelan, S. P. & Chandran, K. (2011). The Ebola virus
756 glycoprotein mediates entry via a non-classical dynamin-dependent macropinocytic pathway.
757 *Virology*, *419*(2), 72–83. https://doi.org/10.1016/j.virol.2011.08.009

758 Nanbo, A., Imai, M., Watanabe, S., Noda, T., Takahashi, K., Neumann, G., Halfmann, P. & Kawaoka, Y.
759 (2010). Ebolavirus Is Internalized into Host Cells via Macropinocytosis in a Viral Glycoprotein-
760 Dependent Manner. *PLoS Pathogens*, *6*(9), e1001121.
761 https://doi.org/10.1371/journal.ppat.1001121

762 Nathan, L., Lai, A. L., Millet, J. K., Straus, M. R., Freed, J. H., Whittaker, G. R. & Daniel, S. (2020).
763 Calcium Ions Directly Interact with the Ebola Virus Fusion Peptide To Promote Structure–Function
764 Changes That Enhance Infection. *ACS Infectious Diseases*, *6*(2), 250–260.
765 https://doi.org/10.1021/acsinfecdis.9b00296

766 Nikić, I., Girona, G. E., Kang, J. H., Paci, G., Mikhaleva, S., Koehler, C., Shymanska, N. V., Santos, C. V.,
767 Spitz, D. & Lemke, E. A. (2016). Debugging Eukaryotic Genetic Code Expansion for Site-Specific
768 Click-PAINT Super-Resolution Microscopy. *Angewandte Chemie International Edition*, *55*(52),
769 16172–16176. https://doi.org/10.1002/anie.201608284

770 Nour, A. M., Li, Y., Wolenski, J. & Modis, Y. (2013). Viral Membrane Fusion and Nucleocapsid Delivery
771 into the Cytoplasm are Distinct Events in Some Flaviviruses. *PLoS Pathogens*, *9*(9), e1003585.
772 https://doi.org/10.1371/journal.ppat.1003585

773 Olsson, M. H. M., Søndergaard, C. R., Rostkowski, M. & Jensen, J. H. (2011). PROPKA3: Consistent
774 Treatment of Internal and Surface Residues in Empirical pKa Predictions. *Journal of Chemical*
775 *Theory and Computation*, *7*(2), 525–537. https://doi.org/10.1021/ct100578z

776 Ou, W., Delisle, J., Konduru, K., Bradfute, S., Radoshitzky, S. R., Retterer, C., Kota, K., Bavari, S., Kuhn,
777 J. H., Jahrling, P. B., Kaplan, G. & Wilson, C. A. (2010). Development and characterization of rabbit
778 and mouse antibodies against ebolavirus envelope glycoproteins. *Journal of Virological Methods*,
779 *174*(1–2), 99–109. https://doi.org/10.1016/j.jviromet.2011.04.003

780 Qin, F., Auerbach, A. & Sachs, F. (2000). A Direct Optimization Approach to Hidden Markov Modeling
781 for Single Channel Kinetics. *Biophysical Journal*, *79*(4), 1915–1927.
782 https://doi.org/10.1016/s0006-3495(00)76441-1

783 Rhoades, E., Ramlall, T. F., Webb, W. W. & Eliezer, D. (2006). Quantification of α-Synuclein Binding to
784 Lipid Vesicles Using Fluorescence Correlation Spectroscopy. *Biophysical Journal*, *90*(12), 4692–
785 4700. https://doi.org/10.1529/biophysj.105.079251

786 Saeed, M. F., Kolokoltsov, A. A., Albrecht, T. & Davey, R. A. (2010). Cellular Entry of Ebola Virus
787 Involves Uptake by a Macropinocytosis-Like Mechanism and Subsequent Trafficking through Early
788 and Late Endosomes. *PLoS Pathogens*, *6*(9), e1001110.
789 https://doi.org/10.1371/journal.ppat.1001110

790 Sakurai, Y., Kolokoltsov, A. A., Chen, C.-C., Tidwell, M. W., Bauta, W. E., Klugbauer, N., Grimm, C.,
791 Wahl-Schott, C., Biel, M. & Davey, R. A. (2015). Two-pore channels control Ebola virus host cell
792 entry and are drug targets for disease treatment. *Science*, *347*(6225), 995–998.
793 https://doi.org/10.1126/science.1258758

794 Salata, C., Calistri, A., Alvisi, G., Celestino, M., Parolin, C. & Palù, G. (2019). Ebola Virus Entry: From
795 Molecular Characterization to Drug Discovery. *Viruses*, *11*(3), 274.
796 https://doi.org/10.3390/v11030274

797 Schwarz, G. (1978). Estimating the Dimension of a Model. *The Annals of Statistics*, *6*(2).
798 https://doi.org/10.1214/aos/1176344136

799 Shi, L., Quick, M., Zhao, Y., Weinstein, H. & Javitch, J. A. (2008). The Mechanism of a
800 Neurotransmitter:Sodium Symporter—Inward Release of Na+ and Substrate Is Triggered by
801 Substrate in a Second Binding Site. *Molecular Cell*, *30*(6), 667–677.
802 https://doi.org/10.1016/j.molcel.2008.05.008

803 Simmons, J. A., D'Souza, R. S., Ruas, M., Galione, A., Casanova, J. E. & White, J. M. (2016). Ebolavirus
804 Glycoprotein Directs Fusion through NPC1 + Endolysosomes. *Journal of Virology*, *90*(1), 605–610.
805 https://doi.org/10.1128/jvi.01828-15

806 Singh, P., Mukherji, S., Basak, S., Hoffmann, M. & Das, D. K. (2022). Dynamic Ca2+ sensitivity
807 stimulates the evolved SARS-CoV-2 spike strain-mediated membrane fusion for enhanced entry.
808 *Cell Reports*, *39*(3), 110694. https://doi.org/10.1016/j.celrep.2022.110694

809 Søndergaard, C. R., Olsson, M. H. M., Rostkowski, M. & Jensen, J. H. (2011). Improved Treatment of
810 Ligands and Coupling Effects in Empirical Calculation and Rationalization of pKa Values. *Journal of*
811 *Chemical Theory and Computation*, *7*(7), 2284–2295. https://doi.org/10.1021/ct200133y

812 Spence, J. S., Krause, T. B., Mittler, E., Jangra, R. K. & Chandran, K. (2016). Direct Visualization of
813 Ebola Virus Fusion Triggering in the Endocytic Pathway. *MBio*, *7*(1), e01857-15.
814 https://doi.org/10.1128/mbio.01857-15

815 Straus, M. R., Tang, T., Lai, A. L., Flegel, A., Bidon, M., Freed, J. H., Daniel, S. & Whittaker, G. R.
816 (2020). Ca 2+ Ions Promote Fusion of Middle East Respiratory Syndrome Coronavirus with Host
817 Cells and Increase Infectivity. *Journal of Virology*, *94*(13). https://doi.org/10.1128/jvi.00426-20

818 Urade, R., Hayashi, Y. & Kito, M. (1988). Endosomes differ from plasma membranes in the
819 phospholipid molecular species composition. *Biochimica et Biophysica Acta (BBA) -*
820 *Biomembranes*, *946*(1), 151–163. https://doi.org/10.1016/0005-2736(88)90468-3

821 Whitt, M. A. (2010). Generation of VSV pseudotypes using recombinant ΔG-VSV for studies on virus
822 entry, identification of entry inhibitors, and immune responses to vaccines. *Journal of Virological*
823 *Methods*, *169*(2), 365–374. https://doi.org/10.1016/j.jviromet.2010.08.006

824 Zaitseva, E., Yang, S.-T., Melikov, K., Pourmal, S. & Chernomordik, L. V. (2010). Dengue Virus Ensures
825 Its Fusion in Late Endosomes Using Compartment-Specific Lipids. *PLoS Pathogens*, *6*(10),
826 e1001131. https://doi.org/10.1371/journal.ppat.1001131

827 Zhao, Y., Ren, J., Harlos, K., Jones, D. M., Zeltina, A., Bowden, T. A., Padilla-Parra, S., Fry, E. E. &
828 Stuart, D. I. (2016). Toremifene interacts with and destabilizes the Ebola virus glycoprotein.
829 *Nature*, *535*(7610), 169–172. https://doi.org/10.1038/nature18615

830

831

832 **Figures**

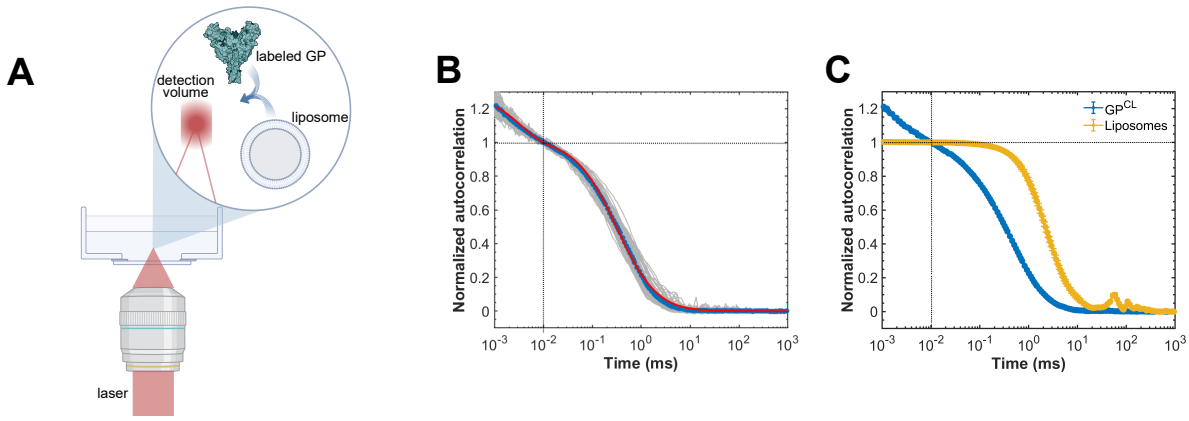

833 Figure 1

834 **Figure 1: FCS reports on GP-membrane interaction.** (**A**) Experimental setup of FCS assay for
835 quantifying GP-membrane interactions. A confocal spot is positioned in a dilute solution of Cy5-
836 labelled GP^{CL} with or without liposomes. Fluorescent particles are detected upon diffusion through
837 the confocal volume. (**B**) Autocorrelation data obtained from unbound Cy5-labelled GP^{CL}. The
838 autocorrelation of individual 5-sec fluorescence intensity traces was calculated (grey curves). The
839 average of 100 autocorrelation curves was calculated (blue) and fitted to a model for a single species
840 diffusing in 3 dimensions with a photophysical dynamics component (red). Accordingly, GP^{CL} has a
841 diffusion time of τ_D = 0.308 ± 0.007 ms. Photophysical dynamics were observed below 10^{-2} ms. (**C**)
842 Autocorrelation curves comparing diffusion times of GP^{CL} (blue) and liposomes (yellow). The diffusion
843 time of liposomes is 2.6 ± 0.2 ms, which is 8-fold longer than GP^{CL}, allowing for identification of
844 membrane-bound and unbound GP^{CL} in solution.

845

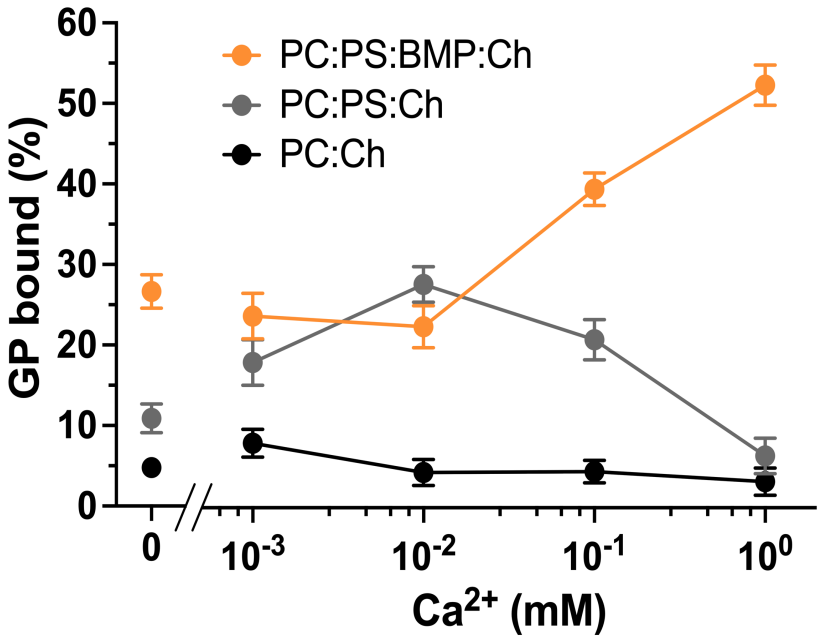

Figure 2

Figure 2: Anionic phospholipids and Ca^{2+} promote GP^{CL}-membrane interaction. The percentage of GP^{CL} bound to liposomes was determined using the FCS assay depicted in **Figure 1A**. Autocorrelation data were obtained from a solution of Cy5-labelled GP^{CL} and unlabelled liposomes and fit to a 3-dimensional diffusion for two species, membrane-bound and unbound GP^{CL} with diffusion times of 0.3 ms and 2.6 ms, respectively (Materials and Methods). Membrane binding to liposomes of varying lipid compositions was measured at pH 5.5 as a function of Ca^{2+} concentration: PC:Ch (black circles), PC:PS:Ch (grey circles) and PC:PS:BMP:Ch (orange circles). Data points reflect the mean ± standard error determined from three sets of measurements.

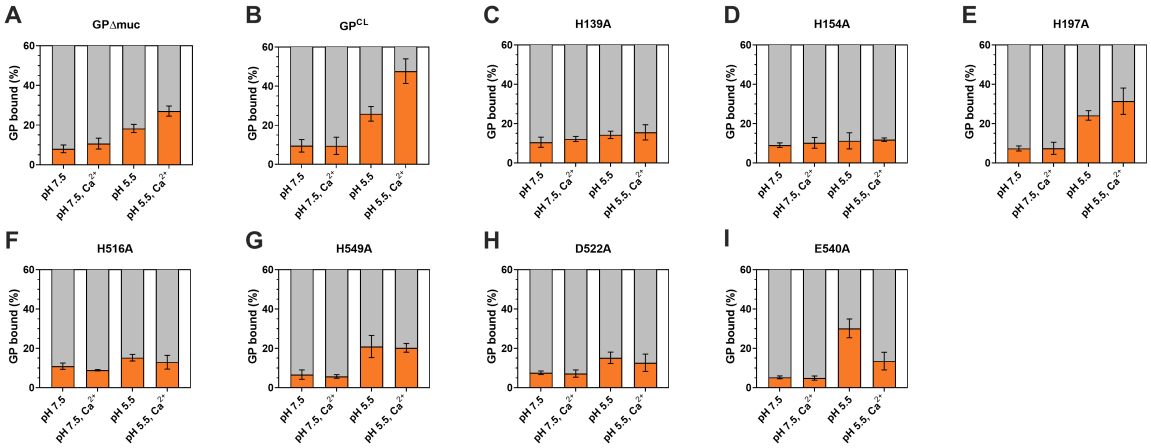

Figure 3

Figure 3: Conserved histidines and acidic residues mediate GP-membrane interaction. Membrane binding of (**A**) GPΔmuc, (**B**) GP^{CL} to PC:PS:BMP:Ch liposomes at neutral and acidic pH in the presence or absence of 1 mM Ca^{2+} is compared with the following mutants: (**C**) H139A, (**D**) H154A, (**E**) H197A, (**F**) H516A, (**G**) H549A, and (**H**) D522A, and (**I**) E540A, respectively. To ensure sensitivity to changes in the percentage of membrane binding of mutant GP^{CL}, a total lipid concentration of 500 µM was used such that a maximum of 50% wild-type GP^{CL} bound to liposomes at low pH in the presence of Ca^{2+}. The mean and standard error were calculated from three independent experiments.

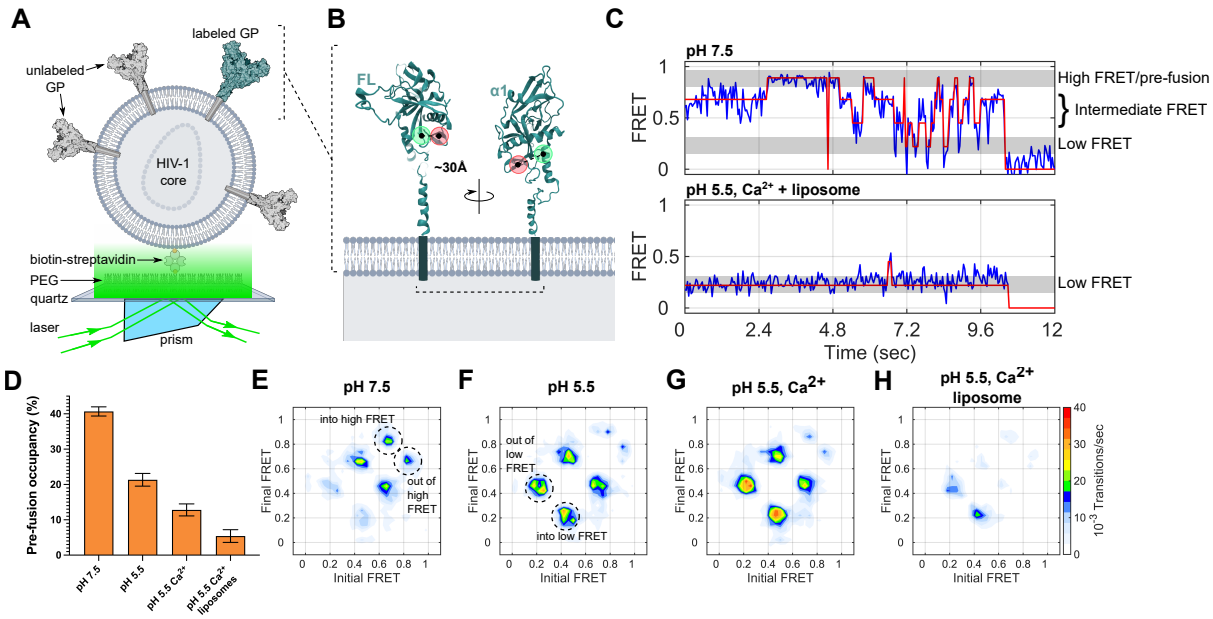

Figure 4

Figure 4: Acidic pH, Ca^{2+} and target membrane regulate GP conformational dynamics. (**A**) Experimental setup for smFRET imaging of pseudovirions labelled with the Cy3 and Cy5 FRET pair. Labelled pseudovirions were immobilized on a PEG-coated quartz microscope slide via a biotin-streptavidin covalent linkage and imaged using prism-based TIRF microscopy. (**B**) Fluorophore attachment positions (red and green circles; residues 501 and 610 in GP2) indicated on a GP protomer (PDB: 5JQ3). The indicated distance of 30 Å was previously determined through MD simulation of the fluorophore-labelled trimer (Das et al., 2020). (**C**) Representative FRET trajectories (blue) of GP^{CL} overlaid with idealization (red) determined through HMM analysis. The trajectory acquired at pH 7.5 (top) shows transitions between the pre-fusion conformation (0.92 FRET), two intermediate-FRET states (0.72 and 0.49), and a low-FRET state (0.24 FRET). In contrast, the FRET trajectory acquired in the presence of liposomes at pH 5.5 and 1 mM Ca^{2+} shows predominantly low FRET indicating a conformation stabilized by the presence of a target membrane. (**D**) Pre-fusion high-FRET state (0.92 FRET) occupancy of GP^{CL} determined under the indicated conditions through HMM analysis. The mean and standard error were calculated from three independent experiments. TDPs displaying the relative frequency of transitions of GP^{CL} at (**E**) pH 7.5, (**F**) pH 5.5, (**G**) pH 5.5 with 1 mM Ca^{2+}, and (**H**) after incubation with PC:PS:BMP:Ch liposomes for 20 min at 37°C, at pH 5.5 and 1 mM Ca^{2+}. Transitions into and out of high- and low-FRET states are depicted in (E) and (F), respectively.

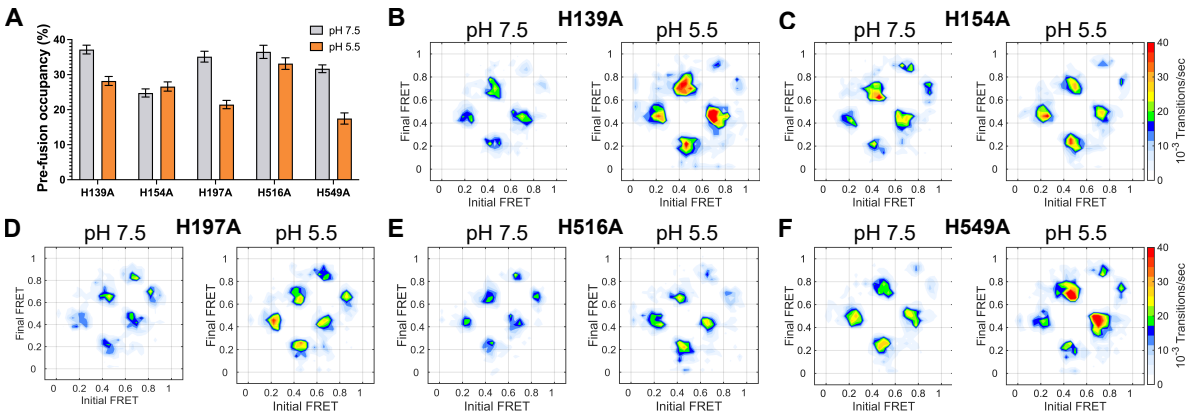

884 Figure 5

885 **Figure 5: Conformational dynamics of GP histidine mutants.** (**A**) Pre-fusion high-FRET state occupancy
886 of GP mutants, determined at pH 7.5 (grey bars) and pH 5.5 (orange bars). The mean and standard
887 error were calculated from three independent experiments. TDPs indicating the relative frequency of
888 conformational transitions at pH 7.5 and pH 5.5, as indicated, for (**B**) H139A, (**C**) H154A, (**D**) H197A, (**E**)
889 H516A, and (**F**) H549A.

890

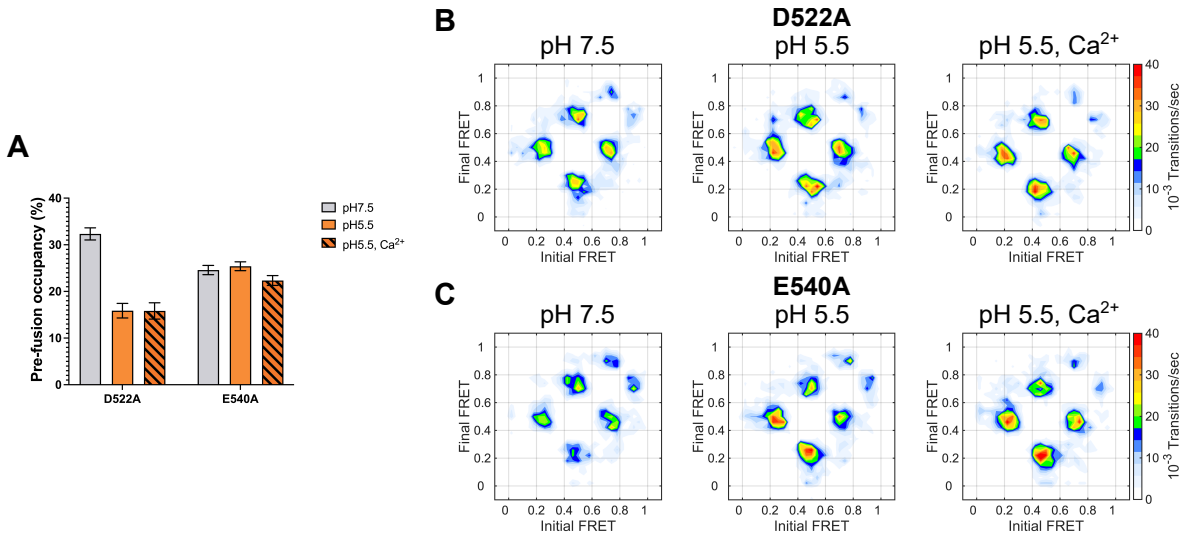

Figure 6

Figure 6: Conformational dynamics of GP with mutations in putative Ca^{2+}-coordinating residues. (**A**) Pre-fusion high-FRET state occupancy of GP mutants, determined at pH 7.5 (grey bars), pH 5.5 (orange bars), and pH 5.5 with 1 mM Ca^{2+} (orange striped bars). The mean and standard error were calculated from three independent experiments. TDPs indicating the relative frequency of conformational transitions determined under the indicated conditions for (**B**) D522A and (**C**) E540A.

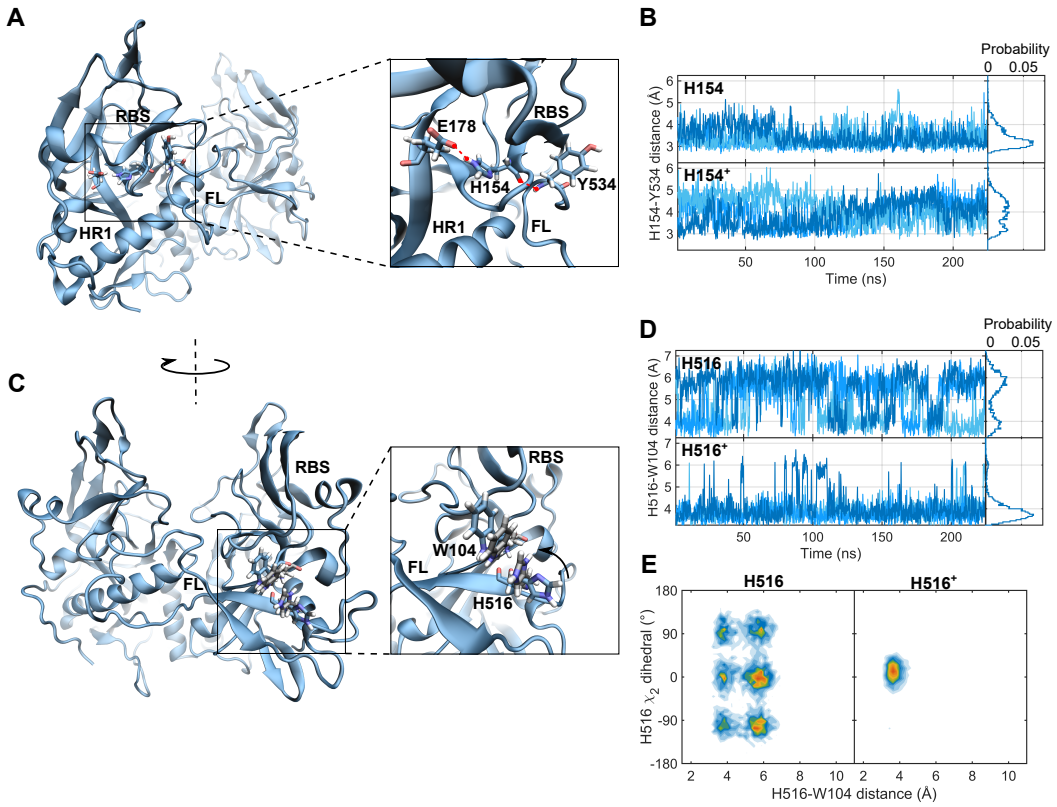

Figure 7

Figure 7: MD simulation provides molecular insights into pH-induced destabilisation of pre-fusion GP. (**A**) The simulation predicted electrostatic interactions between the side chains of H154 and E178, as well as between the backbones of H154 and Y534 in the fusion loop of the neighbouring protomer (red dotted lines). (**B**) The distances between the backbone N of H154 and the backbone carbonyl O of Y534 for each of the three protomers in the GP trimer (three shades of blue) determined from the simulation with (top) deprotonated histidines and (bottom) protonated histidines. Protonation of H154 increases the relative motion of H154 and Y534 as a result of stabilized H154-E178 interaction. (**C**) The simulation also predicts Pi-Pi stacking interaction between H516 in GP2 and W104 in GP1 with both (blue residues) deprotonated and (grey residues) protonated H516. (**D**) Distance trajectories indicating reduced H516-W104 distance under (top) deprotonated and (bottom) protonated conditions for the three protomers in the trimer (three shades of blue). Protonation of H516 (grey residues in (C)) stabilizes the interaction, drawing the two side chains into closer proximity. (**E**) Bivariate histogram of H516-W104 distances and H516 side-chain dihedral angles under (left) deprotonated and (right) protonated conditions. Fewer H516 conformations are available following protonation.

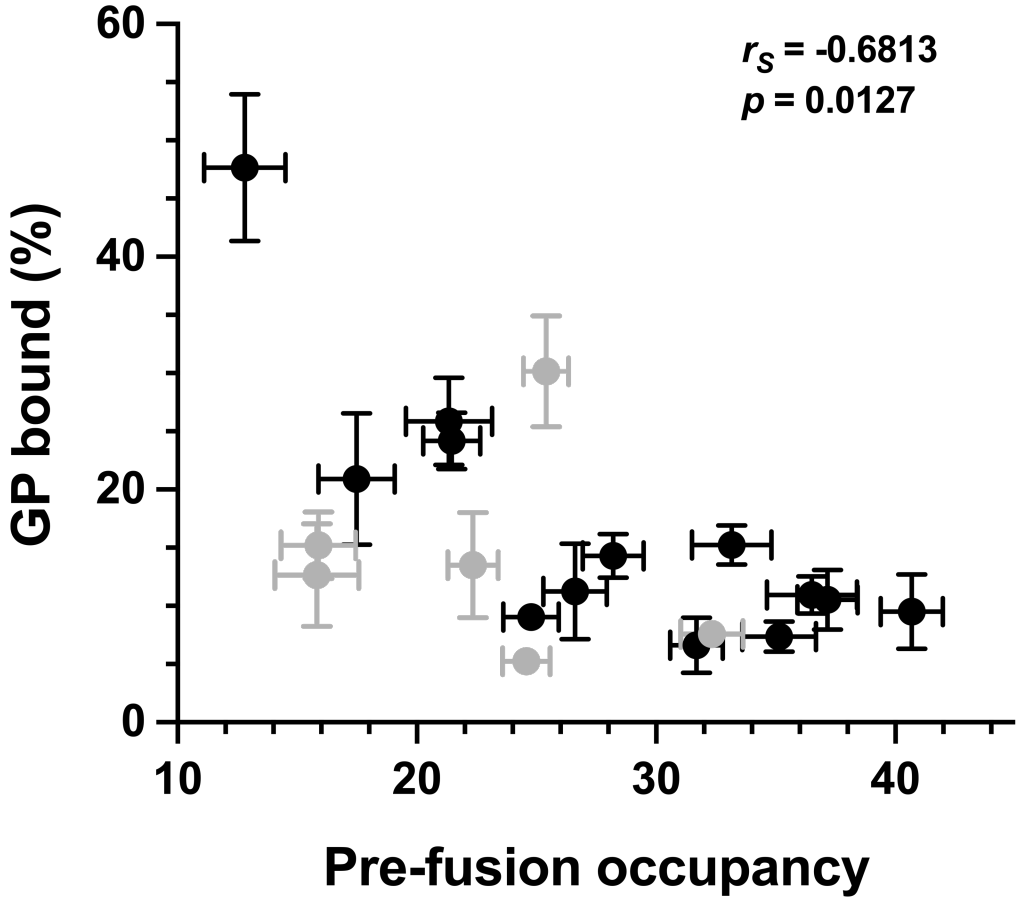

Figure 8

Figure 8: GP occupancy in the pre-fusion high-FRET conformation is inversely correlated with the extent of membrane binding. High-FRET state occupancy was determined through HMM analysis of smFRET trajectories. Membrane binding was determined by FCS. The non-parametric Spearman's correlation coefficient (r_S) and associated p-value are indicated. Data for D522A and E540A (grey points) does not correlate with membrane binding and were excluded from the analysis.